Numerical simulations of thermal convection in rotating spherical shells under laboratory conditions

Ferran Garcia[a,b], Juan Sánchez[a], Marta Net[a,*]

[a]*Dept. de Física Aplicada, Universitat Politècnica de Catalunya, Campus Nord, Mòdul B4, Jordi Girona Salgado 1–3, 08034 Barcelona, Spain.*
[b]*MAG, LRA, Département de Physique, Ecole Normale Supérieure, 24 rue Lhomond, 75005 Paris, France.*

Abstract

An exhaustive study, based on numerical three-dimensional simulations, of the Boussinesq thermal convection of a fluid confined in a rotating spherical shell is presented. A moderately low Prandtl number fluid ($\sigma = 0.1$) bounded by differentially-heated solid spherical shells is mainly considered. Asymptotic power laws for the mean physical properties of the flows are obtained in the limit of low Rossby number and compared with laboratory experiments and with previous numerical results computed by taking either stress-free boundary conditions or quasi-geostrophic restrictions, and with geodynamo models. Finally, using parameters as close as possible to those of the Earth's outer core, some estimations of the characteristic time and length scales of convection are given.

Keywords: Rotating thermal convection, High Rayleigh number, Turbulence, Earth's outer core

1. Introduction

The study of thermal convection in rotating spherical geometries is important for understanding the generation of the magnetic fields of cosmic bodies and in particular in the Earth's outer core. It is widely accepted that they are generated by convection of electrically conducting fluids in their interiors. A recent study (Christensen and Aubert (2006)) predicts that the strength of the magnetic fields is independent of the conductivity and of the rotation rate, and that it is basically controlled by the buoyancy flux. Although it is known that the Earth's magnetic field is driven by both thermal and compositional buoyancy forces (Lister and Buffet (1995); Poirier (2000)) in this paper we focus on the imprint of the former because its knowledge for low Prandtl numbers, σ, is not yet completely understood.

There is a multitude of papers devoted to study the role that thermal convection plays in the dynamics of the celestial bodies. Good reviews can be found in the literature, see for instance Cardin and Olson (1994), Gillet and Jones (2006) and Olson (2011). Therefore we will restrict ourselves to remarking mostly those directly related with temporally chaotic and turbulent flows, with which we compare.

Fully developed thermal convection in a rapidly rotating spherical shell was studied experimentally with water ($\sigma = 7$) and numerically with a quasi-geostrophic model by Cardin and Olson (1994). At a Rayleigh number $Ra = 200Ra_c$, where Ra_c is the critical value of the onset of convection, they found large scale flows with radial variations of the azimuthally averaged velocity, negative (retrograde) near the inner boundary, and positive (prograde), comparable in strength to the former, near the outer. Their results are consistent with a zonal flow maintained by a transfer of energy from the small to the large scales of convection via Reynolds stresses, i.e. by the correlation of the azimuthal component of the velocity field and the cylindrical radial component. This theory was revisited by Gillet and Jones (2006) and Plaut et al. (2008), the latter taking into account the tilt of the convective vortices.

The role of the bulk viscosity and the Ekman friction on the formation of banded zonal structures at weakly nonlinear regimes because of deep convection was studied by Morin and Dormy (2006) with a two-dimensional approximation. They notice that the Ekman pumping tends to produce a large number of bands in the system with the large amplitudes located near the center of the shell. The scale of the transition from dominant bulk viscosity to dominant Ekman friction was found to be $\delta \sim O(\mathcal{L}E^{1/4})$, where $\mathcal{L}$ is the large scale of the axisymmetric flow. The generation of banded atmospheres in the major planets due to turbulent convection was investigated in Aurnou and Olson (2001) and Aurnou and Heimpel (2004), among others, for different radius ratios and boundary conditions.

In a recent experiment with liquid sodium ($\sigma = 0.01$) Shew and Lathrop (2005) got Ekman numbers as low as 10^{-8}, and reached Rayleigh numbers up to 10^9. They found the experimental law for the dimensional time-averaged azimuthal velocity ($|\overline{v_\varphi}|)^d$ as a function of Ra and E close to the inner boundary of the shell, and also derived the scaling relation $\overline{v_\varphi} \sim RaE$ either by balancing Coriolis and buoyancy forces or by supposing that the azimuthal motions come from thermal winds.

The generation of mean zonal flows was analyzed numerically in Christensen (2002) for full three-dimensional calculations with stress-free boundary conditions and Prandtl numbers mainly of order one. It was shown that, at moderate Ra, the

contribution of the mean zonal flow to the total kinetic energy decreases by increasing σ, but when Ra is higher the maximum fraction of the kinetic energy density in the zonal wind is nearly independent of σ. Moreover it was established that the ratio of total kinetic energy density to that in the zonal flow decreases drastically at high Ra due to the loss of geostrophy of the convective columns and the corresponding decorrelation of the Reynolds stresses. In agreement with Cardin and Olson (1994) a prograde mean zonal flow close to the outer boundary and retrograde near the inner sphere was found. Asymptotic power laws computed in the limit of negligible viscosity where used successfully to determine the magnitude of the zonal winds on the surface of the giant gas planets in the absence of magnetic field.

Aubert (2005) and Christensen and Aubert (2006) also obtained differential rotation with non-slip boundary conditions. In addition, the influence of the magnetic fields on the convective and zonal flows was studied in these papers. In the former, it was found that the magnetic field has no direct influence on the variations of the zonal flow along the axis of rotation, but it allows an enhancement of the heat flux by means of the relaxation of the Taylor-Proudman constraint. However, in the second paper, and in agreement with Soderlund et al. (2012), not much different scalings were obtained for magnetic and non-magnetic (Christensen (2002)) rotating convection. Coherent extrapolations in the presence of magnetic fields were reported in Christensen and Aubert (2006). They predicted a magnetic field strength of order 1 mT inside the Earth's outer core.

The zonal circulations in the Earth's outer core were also investigated experimentally in Aubert et al. (2001); Gillet et al. (2007); Shew and Lathrop (2005) for water $\sigma = 7$, gallium $\sigma = 0.023$ and liquid sodium $\sigma = 0.010$. In the experiments the gravity force is supplied by the centrifugal acceleration, thus changing the radial dependence of the buoyancy force to normal to the axis of rotation. However, this modification resulted to be of secondary importance for very high Ra at low and mid-latitudes. Aurnou (2007) compared heat transfer data from recent models of rotating convection. From the analysis of these data he concluded that numerical and laboratory experiments produced different scaling laws. While for the former the relation between the modified Nusselt number (based on the total heat flux) and the modified heat flux-based Rayleigh number is $Nu^* \sim (Ra^*_{Q_T})^{0.55}$, for the latter it is $Nu^* \sim (Ra^*_{Q_T})^{0.29}$ in the regime dominated by the rotation. According to the author the discrepancy could be due to the low conductivity of the materials employed in the outer spherical shells, which could offer a higher resistance to heat transfer than the fluid, or to the existence of a new scenario in which a regime with the heat transfer controlled by the physical properties of the thermal boundary layers exists, that has not yet been achieved.

General scaling laws for the velocity field depending on the total heat flux-based Rayleigh number, Ra_{Q_T}, E, σ and on the slope of the outer sphere were derived in Cardin and Olson (1994). They approximate the inertial state by neglecting the dissipation through the Ekman boundary layers. The velocity, $\tilde{U} \sim E^{1/5}Ra_{Q_T}^{2/5}$, and length scales, $\delta \sim E^{3/5}Ra_{Q_T}^{1/5}$, for the convective vortices in the high Reynolds number regime were

given. In Aubert et al. (2001) scaling laws for the zonal flow, $\hat{U} \sim E^{9/10}Ra_{Q_T}^{4/5}$, were obtained extending the former study by including Ekman friction on the outer boundary. They consider that the kinetic energy is transported from the scale of convective vortices to the large-scale flows through Reynolds stresses, i.e. following a reverse cascade of energy. Then it is dissipated by the zonal flow in the viscous boundary layers. A consequence of this hypothesis is that the energy contained in the zonal flow cannot be significantly higher than the energy contained in the convective vortices. With these scalings they extrapolated values for the Earth's outer core, finding for the radial and azimuthal velocities and for the characteristic length of the convective eddies and zonal flow, $\tilde{U}^d \approx 10^{-3}$ m/s, $\hat{U}^d \approx 10^{-2}$ m/s, $\delta_r = \delta_\varphi \approx 10$ km, respectively.

The same experiment and scaling laws incorporating Ekman pumping and a varying β-effect were re-examined in Gillet et al. (2007), and checked with the data supplied by quasi-geostrophic numerical simulations. At weak supercritical regimes, a quadratic dependence of the zonal flow on convective velocities, $\hat{U} \sim \tilde{U}^2$, was found, reflecting that the zonal flow is driven by the Reynolds stresses if the characteristic length scale corresponds to that established at the onset of convection. For turbulent flows, the amplitude of the zonal motions observed is also larger than that of the convective flows. In this regime they took as characteristic azimuthal scale the Rhines scale, $\delta_\beta \sim \sqrt{\hat{U}/\beta}$, associated with the radial shear of the mean flow. They found that the balance between the Reynolds stress and the Ekman friction is $\hat{U} \sim \tilde{U}^{4/3}$.

Recently, from a dataset of several numerical dynamo models, Stelzer and Jackson (2013) have analyzed, by leaving one parameter out and cross-validation, the results of other authors. They found that diffusion dependent parameters are needed for scaling the flow velocity and the magnetic field strength. Moreover King and Buffett (2013) have found $l \sim E^{1/3}$ and $U \sim C^{1/2}E^{1/3}$ for typical length scales and speeds, respectively. They come from theoretical scaling analysis (balances between rotation, viscosity and buoyancy), which are fitted to several dynamo simulation data. In the latter formula $C = Ra(Nu-1)\sigma^{-2}$ accounts for the convective power. According to the authors, there are some evidences that geodynamo simulations with magnetic Prandtl numbers tending to zero would lead to a new regime in which large scale convection and Lorentz forces would be more important than viscosity.

The frequency spectra of the temperature observed by Shew and Lathrop (2005) shows an abrupt change in the slope at a high frequency (knee frequency f_c). It was related with the inverse cascade of energy dissipation pointed out by Aubert et al. (2001) and Gillet et al. (2007) in the framework of the two-dimensional turbulence. Shew and Lathrop (2005) suggested that for frequencies lower than f_c the temperature fluctuations are due to an inverse cascade of energy from the scale of convective flows to the largest scales up to the size of the domain.

Despite the power of modern computers full three-dimensional simulations at high Reynolds numbers with an acceptable wall-clock CPU time must be run using parameters that are far from those of the dynamics of the planetary liquid

cores, or limit its number to study a particular phenomenon in a very well planed way. In any case nowadays the simulations are far from reaching the Ekman and Rayleigh numbers of the Earth's outer core. In this paper we adopt the first approach, and extend the previous stress-free numerical study of Christensen (2002), by using non-slip boundary conditions, mainly the lower Prandtl number value $\sigma = 0.1$ and the radius ratio of the Earth's outer core $\eta = 0.35$. Our simulations are performed for four Ekman numbers, E, the larger being $E = 10^{-4}$, which, although it is far from those needed for real applications, is sufficiently small to be in the asymptotic regime of the onset of convection (see Garcia et al. (2008)). In addition the values used allow us to compare with other authors. The location of the convection and the flow patterns, as well as the asymptotic laws of the flow properties in the regime of fully developed convection, are studied. The results are mainly confronted with the experimental data and scaling laws of Aubert et al. (2001); Shew and Lathrop (2005); Gillet et al. (2007). In addition, the fittings are used to extrapolate physical properties to a situation similar to that of the present day Earth's outer core.

The study is organized as follows: In Sec. 2, the formulation of the problem and the definition of the output data are introduced. Sec. 3 contains the validation of the numerical results. The study of the variation of the location of the convection with Ra is performed in Sec. 4 by computing relevant physical properties at different collocation points inside the shell. The purpose of Sec. 5 is to find scaling relations as functions of the diffusivity-free Rayleigh number, and to compare them with the equivalent limits including magnetic field. A comparison with the scaling laws derived from previous experimental studies is performed in Sec. 6. In Sec. 7 the fittings are used to extrapolate to the Earth's outer core values, and the final conclusions are discussed in Sec. 8. The Appendix contains a summary of the properties analyzed in the preceding sections.

2. The equations and output data

We consider the thermal convection of a fluid filling the gap between two concentric spheres differentially heated, rotating about an axis of symmetry with constant angular velocity $\mathbf{\Omega} = \Omega\mathbf{k}$, and subject to radial gravity $\mathbf{g} = -\gamma\mathbf{r}$, where γ is constant and $\mathbf{r}$ the position vector. The mass, momentum and energy equations are written in the rotating frame of reference. The units are $d = r_o - r_i$ for the distance , $\nu^2/\gamma\alpha d^4$ for the temperature, and d^2/ν for the time. In the previous definitions r_i and r_o are the inner and outer radii, respectively, ν the kinematic viscosity, and α the thermal expansion coefficient.

We use the Boussinesq approximation and the solenoidal velocity field is expressed in terms of toroidal, Ψ, and poloidal, Φ, potentials

$$\mathbf{v} = \mathbf{\nabla} \times (\Psi\mathbf{r}) + \mathbf{\nabla} \times \mathbf{\nabla} \times (\Phi\mathbf{r}). \quad (1)$$

Consequently, the equations for both potentials, and the temperature perturbation, $\Theta = T - T_c$, from the conduction state

$\mathbf{v} = \mathbf{0}, T = T_c(r)$, with $r = |\mathbf{r}|$, are

$$\left[(\partial_t - \nabla^2)L_2 - 2E^{-1}\partial_\varphi\right]\Psi = -2E^{-1}Q\Phi - \\ - \mathbf{r} \cdot \mathbf{\nabla} \times (\omega \times \mathbf{v}), \quad (2)$$

$$\left[(\partial_t - \nabla^2)L_2 - 2E^{-1}\partial_\varphi\right]\nabla^2\Phi + L_2\Theta = 2E^{-1}Q\Psi + \\ + \mathbf{r} \cdot \mathbf{\nabla} \times \mathbf{\nabla} \times (\omega \times \mathbf{v}), \quad (3)$$

$$\left(\sigma\partial_t - \nabla^2\right)\Theta - Ra\,\eta\,(1-\eta)^{-2}r^{-3}L_2\Phi = -\sigma(\mathbf{v} \cdot \mathbf{\nabla})\Theta, \quad (4)$$

where $\omega = \mathbf{\nabla} \times \mathbf{v}$ is the vorticity.

The parameters of the problem are the Rayleigh number Ra, the Prandtl number σ, the Ekman number E, and the radius ratio η. They are defined by

$$Ra = \frac{\gamma\alpha\Delta T d^4}{\kappa\nu}, \quad E = \frac{\nu}{\Omega d^2}, \quad \sigma = \frac{\nu}{\kappa}, \quad \eta = \frac{r_i}{r_o}, \quad (5)$$

where κ is the thermal diffusivity, and $\Delta T > 0$ the difference of temperature between the inner and outer boundaries.

The operators L_2 and Q are defined by $L_2 \equiv -r^2\nabla^2 + \partial_r(r^2\partial_r)$, $Q \equiv r\cos\theta\nabla^2 - (L_2 + r\partial_r)(\cos\theta\partial_r - r^{-1}\sin\theta\partial_\theta)$, (r, θ, φ) being the spherical coordinates, with θ measuring the colatitude, and φ the longitude. When non-slip perfect thermally conducting boundaries are used

$$\Phi = \partial_r\Phi = \Psi = \Theta = 0 \quad \text{at} \quad r = r_i, r_o. \quad (6)$$

The conduction state in non-dimensional units is $T_c(r) = T_0 + Ra\,\eta/\sigma(1-\eta)^2 r$.

The equations are discretized and integrated as described in Garcia et al. (2010) and references therein. The potentials and the temperature perturbation are expanded in spherical harmonics in the angular coordinates, and in the radial direction a collocation method on a Gauss-Lobatto mesh is used.

Since we are interested in comparing our results with those of different authors, several types of output data are analyzed. The local output data consist of time series of selected variables taken at representative points of the domain (see Sec. 4). Global data correspond to physical properties averaged over the whole volume, or on the surface of a sphere. The first global data used here is the Nusselt number, defined as the ratio of the average of the total radial heat flux to the conductive heat flux, both through the outer surface,

$$Nu = \frac{\langle J_T(r_o, \theta, \varphi)\rangle_S}{\langle J_c(r_o)\rangle_S} = -(\sqrt{2}\sigma/2\eta Ra)\partial_r\Theta_0^0(t, r_o) + 1, \quad (7)$$

the brackets $\langle\rangle_S$ mean the surface integral evaluated at $r = r_o$, and Θ_0^0 is the zero degree and order amplitude of the spherical harmonic coefficient of the temperature perturbation expansion. The second is the volume-averaged kinetic energy density $K = \frac{1}{2}\langle|\mathbf{v}|^2\rangle_V$, called from now on kinetic energy density (KED) for simplicity, i.e.

$$K = \frac{1}{V} \int_V \frac{1}{2}(\mathbf{v} \cdot \mathbf{v})\, dv = (3\sqrt{2}/4(r_o^3 - r_i^3)) \int_{r_i}^{r_o} r^2[v^2]_0^0(r, t)\, dr. \quad (8)$$

3

The previous volume integral can also be computed for either the toroidal, $\boldsymbol{\nabla} \times (\Psi\mathbf{r})$, or the poloidal, $\boldsymbol{\nabla} \times \boldsymbol{\nabla} \times (\Phi\mathbf{r})$, component of the velocity field, giving rise to either the toroidal, K_t, or the poloidal, K_p, KEDs. The axisymmetric, K_a, and the non-axisymmetric, K_{na}, KEDs can also be defined by modifying the velocity field of Eq. (8). They are based, respectively, on the $m = 0$ or the $m \neq 0$ modes of the spherical harmonic expansion of the potentials Ψ and Φ. From these volume-averaged kinetic energy densities the Reynolds number is obtained as $Re_* = \sqrt{2K_*}$, and the Rossby number as $Ro_* = Re_* E$, where $*$ means the part of the total energy taken into account. Whatever the data d_s be (local or global) a time series of the form $(t_i, d_s(t_i))$, $i = 1, \ldots, N$ can be obtained, and its time average (mean value)

$$\overline{d_s} = \frac{1}{\Delta t} \int_t^{t+\Delta t} d_s \, dt, \tag{9}$$

and relative variance or relative root-mean-square (r.m.s.) d_s deviation

$$\sigma_{d_s} = \frac{\sqrt{\overline{(d_s - \overline{d_s})^2}}}{\overline{d_s}} \tag{10}$$

can be computed. The symbols and the definition of the physical properties that will be studied along this paper are summarized in Table 12 of the Appendix.

3. Validation and accuracy of the results

The numerical solutions can be computed by imposing a m_d-fold azimuthal symmetry. This is accomplished by only retaining the modes with wave number $m = km_d$, $k \in \mathbb{Z}$ for a given m_d, in the truncated spherical harmonics expansion of the unknowns. Besides of reducing the numerical effort for obtaining time-averaged properties of strongly supercritical flows, the constrain on the symmetry can also be used to find existing unstable flows.

The first solution, corresponding to $Ra = 2 \times 10^5$ with $E = 10^{-4}$, is computed by starting from an initial condition with velocity $\mathbf{v} = \mathbf{0}$, and temperature

$$T_B(r, \theta, \varphi) = \frac{r_i r_o}{r} - r_i + \frac{2A}{\sqrt{2\pi}}(1 - x^2)^3 P_m^m(\theta) \cos m\varphi, \tag{11}$$

with $A = 0.1$, $x = 2r - r_i - r_o$, $m = 6$, and $P_m^m(\theta) = \sqrt{(2m+1)!!/2(2m)!!} \sin^m \theta$ the normalized associated Legendre function of order and degree m. The solution tends, after an abrupt transient, to an azimuthal travelling wave of wave number $m = 6$. At higher Ra the calculations are started from the solution computed at the previous lower Ra. For $E = 3.162 \times 10^{-5}$, the first solution is computed using again the initial condition given in Eq. (11), but with critical wave number $m = 8$, and at $E = 8.165 \times 10^{-6}$ with $m = 12$. The resolution is increased from time to time in order to look into spatial discretization errors (see Tables 1 and 2). The initial transients are discarded until a stationary pattern is reached or until the time-averaged properties and the fundamental frequencies do not substantially change.

For $E = 10^{-4}$, $\sigma = 0.1$ and small Ra, the solutions are obtained firstly without symmetry assumptions ($m_d = 1$), that is by using all the spherical harmonics in the expansions of the functions. At about Ra ten times supercritical or greater, a two-fold longitudinal symmetry is assumed (only the even modes in the spherical expansions are retained) because we have checked that this does not change significantly the mean values of the fields, and nearly halves the computational time. In Tables 1 and 2, several space and time-averaged physical properties, computed with $m_d = 8$, $m_d = 4$, $m_d = 2$ and $m_d = 1$, are listed for several solutions at different Ekman numbers, in order to show the differences caused by the use of each symmetry. Different spatial resolutions are also used for checking the accuracy of the results. Notice in the second table that only K_p^a changes significantly with the change of symmetry, and that it is one or two orders of magnitude lesser than the others, so its contribution hardly modifies the axisymmetric KED. For this reason K_t^a will be used as an estimator of the KED stored in the zonal flow.

Finally, in order to check the correct computation of the physical magnitudes, some volume and time-averaged physical properties are compared in Table 3 with those of Christensen (2002) for two values of E. They are computed by using his parameters and boundary conditions. In addition, the mean ratio of KED to its non-axisymmetric contribution (shown in Fig. 6c of Christensen (2002)) is included. In our case both solutions are obtained without symmetry assumptions ($m_d = 1$), although in Christensen (2002) a two-fold symmetry is imposed for the solutions corresponding to $E = 10^{-4}$. The agreement is very good, taking into account that it is impossible to capture exactly the same temporal register for non-periodic flows.

4. Location of convection

Some time-averaged local quantities, extracted from a sequence of solutions obtained by increasing Ra for $E = 10^{-4}$, are analyzed in this section to quantify the variation of the location of convection with Ra up to approximately $10 Ra_c$. The time-averaged quantities are extracted from representative collocation points p_i, $i = 1, \ldots, 9$, whose positions are sketched in Fig. 1. Their spherical coordinates are given in the figure caption.

In Fig. 2, the time-averaged azimuthally-averaged azimuthal component of the velocity field, $\langle \overline{v_\varphi} \rangle$ (from now on mean zonal flow), at the collocation points p_i, $i = 1, \ldots, 9$, is plotted versus Ra. The rate of generation of $\langle \overline{v_\varphi} \rangle$ is faster in the neighborhood of the tangent cylinder depicted in Fig. 1. For $Ra < 5 \times 10^5$, only a weak retrograde mean zonal flow very close to the internal part of the cylinder is generated (see the situation of points p_3 and p_4 in the figure), however in the external part the generation is more than twice that of the former (see points p_5 and p_7). As Ra is increased, the mean zonal circulation becomes stronger and spreads affecting most of the shell, although maintaining a weak value (see points p_8, p_6, p_1 and p_2). The intensity of the retrograde mean zonal flow weakens from the tangent cylinder to the rotation axis and to the outer sphere. In fact, near the outer boundary at low and mid latitudes, there

$$E = 10^{-4}$$

Ra/Ra_c	$\overline{Re} \times 10^{-2}$	$\overline{Re_p} \times 10^{-2}$	$\overline{Nu}$	$\overline{K/K_{na}}$	σ_{K_p}	N_r	L	m_d
5.39	2.634	1.082	1.286	1.968	0.326	32	54	2
5.39	2.599	1.064	1.274	1.873	0.214	32	54	1
5.39	2.598	1.066	1.274	1.870	0.210	50	84	1
10.78	6.782	3.119	2.103	1.868	0.173	50	84	2
10.78	6.762	3.128	2.094	1.770	0.135	50	84	1
26.94	13.60	7.596	3.907	1.385	0.138	50	84	2
26.94	13.68	7.594	3.905	1.338	0.094	50	84	1
26.94	13.89	7.765	3.918	1.410	0.143	70	128	2
37.70	16.38	9.608	4.725	1.251	0.123	50	84	2
37.70	16.86	9.933	4.738	1.249	0.115	70	128	2
53.88	21.45	13.03	5.770	1.152	0.085	80	160	2
53.88	21.42	13.01	5.820	1.116	0.060	80	160	1

$$E = 3.162 \times 10^{-5}$$

Ra/Ra_c	$\overline{Re} \times 10^{-2}$	$\overline{Re_p} \times 10^{-1}$	$\overline{Nu}$	$\overline{K/K_{na}}$	σ_{K_p}	N_r	L	m_d
3.14	1.725	6.507	1.100	1.926	0.314	32	54	2
3.14	1.746	6.511	1.101	1.971	0.298	50	84	2
78.50	39.61	189.2	7.431	2.090	0.181	70	128	4
78.50	39.10	197.9	7.618	1.702	0.138	70	128	2
78.50	38.61	202.5	7.717	1.564	0.126	70	148	2
78.50	40.54	209.7	7.855	1.629	0.128	80	192	2

$$E = 8.165 \times 10^{-6}$$

Ra/Ra_c	$\overline{Re} \times 10^{-3}$	$\overline{Re_p} \times 10^{-3}$	$\overline{Nu}$	$\overline{K/K_{na}}$	σ_{K_p}	N_r	L	m_d
41.62	4.219	1.773	5.207	2.311	0.166	80	192	8
41.62	3.873	1.820	5.374	1.787	0.137	70	128	4
41.62	4.379	1.819	5.442	2.319	0.151	80	192	4

Table 1: Time-averaged Reynolds number, $\overline{Re}$, its poloidal contribution, $\overline{Re_p}$, Nusselt number, $\overline{Nu}$, ratio between KED to its non-axisymmetric contribution, $\overline{K/K_{na}}$, and relative variance of the poloidal KED, σ_{K_p}, for several solutions computed with different numerical radial resolution, N_r, spherical harmonic degree, L and imposed m_d-fold azimuthal symmetry. In all cases $\sigma = 0.1$.

is a region of prograde mean zonal flow whose strength also increases with Ra (see point p_9 and Fig. 3), becoming comparable to the retrograde circulations calculated at p_8. The existence of opposite zonal flows indicate that the shear stresses in the transition zone, estimated near $r = r_i + 0.5(r_o - r_i)$ are very strong. The prograde differential rotation near the equator at the outer surface was already found by Cardin and Olson (1994) and Aubert et al. (2001) in water and gallium experiments, by Tilgner and Busse (1997) in three-dimensional numerical simulations with stress-free boundaries, and by Cardin and Olson (1994) in quasi-geostrophic simulations with non-slip boundaries and Prandtl numbers $\sigma = 0.1, 1, 7, 10$.

Figure 1: Meridional section of the spherical shell taken at $\varphi = 0$ showing the points p_i, $i = 1, \cdots, 9$, where the time-averaged physical properties are monitored. Their colatitudinal coordinates are $\theta \simeq \pi/8$, $\theta \simeq \pi/4$, and $\theta \simeq 3\pi/8$, and the radial are $r = r_i + (r_o - r_i)/7$, $r = r_i + (r_o - r_i)/2$, and $r = r_i + 6(r_o - r_i)/7$.

In Fig. 3 the snapshots of the azimuthally-averaged azimuthal component of the velocity field (zonal flow), $\langle v_\varphi \rangle$, are taken in meridional sections for five representative Rayleigh numbers, $Ra = 3.42 \times 10^5$, 5.1×10^5, 7.5×10^5, 10^6, and 2×10^6. The scale of greys (colors online) is different for each figure. Black and white (blue and red) colors mean retrograde and prograde zonal flows, respectively. In the sequence, the above mentioned tendency of the negative circulations to expand to wider regions of the spherical shell, and the existence of positive circulations
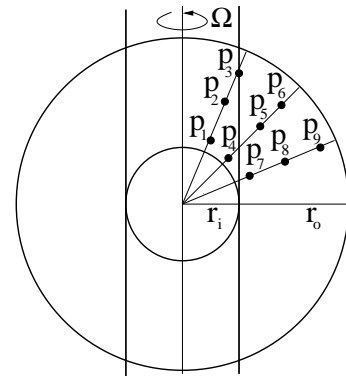
5

$$E = 10^{-4}$$

Ra/Ra_c	$\overline{K} \times 10^{-4}$	$\overline{K_t^a} \times 10^{-4}$	$\overline{K_t^{na}} \times 10^{-4}$	$\overline{K_p^a} \times 10^{-1}$	$\overline{K_p^{na}} \times 10^{-3}$	N_r	L	m_d
5.39	3.5039	1.6204	1.2823	13.654	5.8763	32	54	2
5.39	3.3900	1.5371	1.2800	7.9091	5.6504	32	54	1
5.39	3.3885	1.5349	1.2794	7.9426	5.6639	50	84	1
10.78	23.058	10.270	7.8875	201.03	46.990	50	84	2
10.78	22.895	9.7083	8.2735	113.51	48.000	50	84	1
26.94	92.683	23.484	40.218	1410.4	275.71	50	84	2
26.94	93.608	22.485	42.224	762.55	281.37	50	84	1
26.94	96.680	25.580	40.795	1543.0	287.62	70	128	2
37.70	134.36	23.690	64.338	2357.2	439.71	50	84	2
37.70	142.42	24.982	67.946	2589.7	469.05	70	128	2
53.88	230.20	25.153	119.95	4639.7	804.65	80	160	2
53.88	229.41	21.145	123.60	2386.8	822.71	80	160	1

$$E = 3.162 \times 10^{-5}$$

Ra/Ra_c	$\overline{K} \times 10^{-4}$	$\overline{K_t^a} \times 10^{-3}$	$\overline{K_t^{na}} \times 10^{-3}$	$\overline{K_p^a}$	$\overline{K_p^{na}} \times 10^{-3}$	N_r	L	m_d
3.14	1.5047	6.9264	5.9502	7.6585	2.1623	32	54	2
3.14	1.5396	7.2993	5.9285	7.3023	2.1611	50	84	2
78.50	786.00	3861.6	2195.4	141679.	1661.2	70	128	4
78.50	765.41	3004.0	2683.0	78414.	1888.6	70	128	2
78.50	746.17	2542.4	2859.5	82921.	1976.2	70	148	2
78.50	822.62	3017.7	3000.7	92269.	2115.5	80	192	2

$$E = 8.165 \times 10^{-6}$$

Ra/Ra_c	$\overline{K} \times 10^{-6}$	$\overline{K_t^a} \times 10^{-6}$	$\overline{K_t^{na}} \times 10^{-6}$	$\overline{K_p^a} \times 10^{-4}$	$\overline{K_p^{na}} \times 10^{-6}$	N_r	L	m_d
41.62	7.5129	3.2108	2.6392	4.9787	1.613	70	128	4
41.62	8.9253	4.9370	2.4068	6.2713	1.519	80	192	8
41.62	9.6000	5.3407	2.5964	5.6730	1.606	80	192	4

Table 2: Time-averaged total KED, $\overline{K}$, axisymmetric toroidal KED, $\overline{K_t^a}$, non-axisymmetric toroidal KED, $\overline{K_t^{na}}$, axisymmetric poloidal KED, $\overline{K_p^a}$, non-axisymmetric poloidal KED, $\overline{K_p^{na}}$, for several solutions computed with the resolutions and symmetries of Table 1. In all cases $\sigma = 0.1$
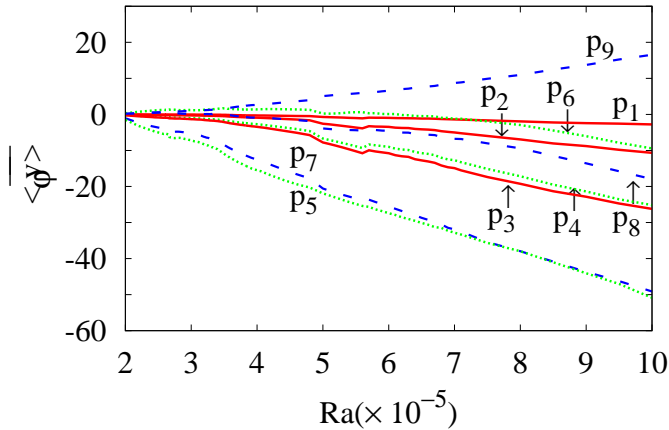
Figure 2: Time averaged azimuthally-averaged azimuthal component of the velocity field $\langle \overline{v_\varphi} \rangle$, at the collocation points of Fig. 1, plotted versus Ra. The radii are $r = r_i + (r_o - r_i)/7$ at p_1, p_4 and p_7, $r = r_i + (r_o - r_i)/2$ at p_2, p_5 and p_8, and $r = r_i + 6(r_o - r_i)/7$ at p_3, p_6 and p_9, and solid/dotted/dashed (red/green/blue colors online) lines mean: $\theta = \pi/8$, $\theta = \pi/4$ and $\theta = 3\pi/8$, respectively.
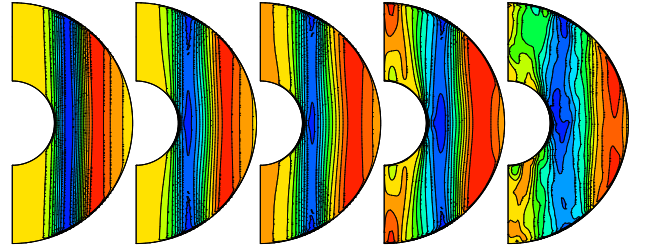
Figure 3: From left to right, contour plots of snapshots of the zonal flow $\langle v_\varphi \rangle$ on meridional sections at $Ra = 3.42 \times 10^5$, $Ra = 5.1 \times 10^5$, $Ra = 7.5 \times 10^5$, $Ra = 10^6$, and $Ra = 2 \times 10^6$, respectively.

at low and mid latitudes close to the outer boundary, can also be observed. This expansion is quantified in Table 4, where it can be seen that the radial position of $\langle v_\varphi \rangle = 0$ in the equator travels from $r = r_i + 0.4(r_o - r_i)$ to $r = r_i + 0.525(r_o - r_i)$ when Ra varies from $Ra = 3.42 \times 10^5$ to $Ra = 2 \times 10^6$. The maximum and minimum values of $\langle v_\varphi \rangle$ are also written down on the same table, together with the coordinates where they take place. Notice that, at least at the instant of time considered, both extrema are located close to the outer surface, and, while the latitude of the maximum of the retrograde flows scarcely changes, that of the prograde moves from 43º to 31º, i.e. the flows be-

$$E = 3 \times 10^{-4}$$

Results	Ra/Ra_c	$\overline{Re}$	$\overline{Re_p}$	$\overline{Nu}$	K/K_{na}	σ_{K_p}	N_r	L	m_d
GNS13	5.36	40.6	12.6	1.338	2.90	0.17	32	54	1
Chr02	5.36	41.0	12.6	1.342	–	0.25	33	53	1
GNS13	6.7	59.9	17.0	1.470	3.80	0.33	32	54	1
Chr02	6.7	60.9	15.3	1.454	–	0.34	33	53	1

$$E = 10^{-4}$$

Results	Ra/Ra_c	Re	Re_p	Nu	K/K_{na}	σ_{K_p}	N_r	L	m_d
GNS13	4.3	39.7	8.43	1.134	4.84	0.28	32	53	1
Chr02	4.3	41.1	8.2	1.123	5	0.33	33	53	2

Table 3: Comparison of our results for $\sigma = 1$ and stress-free boundary conditions with those of Christensen (2002). The parameters, properties and resolutions are the same as in Table 1.

Ra	$\langle v_\varphi \rangle_{\max}$	$(r_{\max} - r_i)/d$	$\theta_{\max}\text{o}$	$\langle v_\varphi \rangle_{\min}$	$(r_{\min} - r_i)/d$	$\theta_{\min}\text{o}$	$r_{+/-} - r_i$
3.42×10^5	2.42×10^1	0.975	46.59	-6.53×10^1	0.975	29.65	0.4
5.1×10^5	5.72×10^1	0.975	48.71	-1.64×10^2	0.975	27.53	0.462
7.5×10^5	9.12×10^1	0.975	52.94	-2.93×10^2	0.975	27.53	0.487
10^6	1.06×10^2	0.975	57.21	-3.63×10^2	0.975	27.91	0.5
2×10^6	4.30×10^2	0.975	58.60	-1.04×10^3	0.975	30.70	0.525

Table 4: Maximum/minimum value of $\langle v_\varphi \rangle$ and coordinates $(r_{\max/\min} - r_i, \theta_{\max/\min})$ where they are located for the five solutions shown in Fig. 3. The radius $(r_{+/-} - r_i)/d$ indicates the change of sign of $\langle v_\varphi \rangle$ in the equatorial plane.

come progressively confined to lower latitudes. When Coriolis is no longer the dominant force, the latitudinal profile of the zonal flow close to the outer boundary depens mainly on the deepness of the convective layer Aurnou et al. (2007), and the boundary conditions. With increasing Ra, prograde polar circulations start to develop, and the validity of the Taylor-Proudman constraint is progressively lost. At $Ra = 2 \times 10^6$ ($Ra \approx 10Ra_c$ with $Ra_c = 1.856 \times 10^5$), the equatorial symmetry is already broken although the flows still maintain a recognizable columnar structure.

5. Numerical asymptotic limit

As a first step the mean Reynolds, $\overline{Re}$, and Nusselt, $\overline{Nu}$, numbers, and zonal flow, $-\langle \overline{v_\varphi} \rangle$, are plotted versus the heat flux-based Rayleigh number, $Ra_Q = Ra(\overline{Nu} - 1)$, in Fig. 4 for $\sigma = 0.1$ and $E = 10^{-4}$ (empty squares), $E = 3.162 \times 10^{-5}$ (stars) and $E = 8.165 \times 10^{-6}$ (crosses), $\sigma = 0.025$ and $E = 10^{-5}$ (black squares), and $\sigma = 1$, $E = 3.162 \times 10^{-5}$ (circles).

Two regimes can be observed, in Figs 4a,b, with two very different slopes in that of $\overline{Nu}$, and a short transition zone between them. For a fixed Prandtl number ($\sigma = 0.1$ in this case), the mean Reynolds and Nusselt numbers show a power dependence for high and low Rayleigh numbers. In the first case the curves of $\overline{Re}$ tend to collapse, while those of $\overline{Nu}$ become almost parallel (see the curves of empty squares, asterisks and pluses). On the other hand, fluids with other σ values (black squares and circles) follow the same type of behavior, with a slightly different slope. Since we are interested in the very high Re regime ($Re > 1000$), it is possible to collapse all the curves if they are depicted in front of a diffusion independent parameter

Ra_Q^* (defined below). It is important to realize that this procedure is only possible for high Re since Fig 4 (and the equivalent but plotted versus Ra, not included here) also shows the dependence of the low Re regime on the diffusivities. A third regime can be differentiated in Fig 4c in which the zonal flow becomes saturated, but the heat flux and the modulus of the velocity field continue increasing its value.

To quantify the global balance of the forces acting on the fluid per unit mass, we have also evaluated, as in Soderlund et al. (2012), their mean volume-averaged value, defined as in Eq. 8, for several solutions corresponding to the regimes above mentioned. The results are included in Table 5. They show that at low Ra and at leading order, the dynamics comes from the balance between the Coriolis force and the modified pressure gradient with heat transported mainly by conduction. The other forces are two orders of magnitude smaller. At very high Ra (see $E = 3.162 \times 10^{-5}$) the inertial force is needed to balance the modified pressure gradient, and the buoyancy force becomes as large as the Coriolis force. When the zonal flow flattens out the inertial overcomes the Coriolis term, and the ratio between the inertial and viscous forces becomes constant.

The time-averaged physical properties and scaling laws computed in this section are compared with the numerical results obtained by Christensen (2002) with stress-free boundary conditions for $\sigma = 0.3$ and 1, and with those of Christensen and Aubert (2006) in convection-driven dynamos with non-slip boundaries and σ ranging from 0.1 to 10. In these articles it was already assumed that the scaling laws of the volume-averaged physical parameters could be written at low E and high Ra as functions of the modified heat flux-based Rayleigh number $Ra_{Q_T}^*$ in the former and Ra_Q^* in the latter, because for strongly supercritical Ra the convection is maintained predominantly by
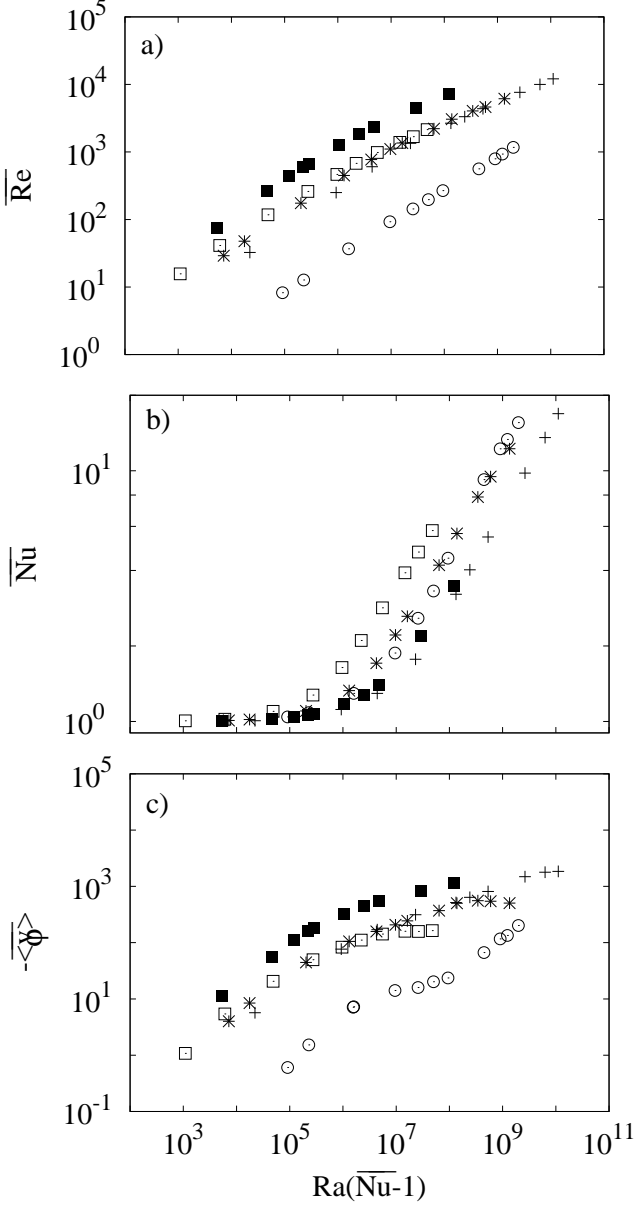
Figure 4: (a) Mean Reynolds number, $\overline{Re}$, (b) Nusselt number, $\overline{Nu}$, and (c) zonal flow $-\langle\overline{v_\varphi}\rangle$ versus $Ra(\overline{Nu}-1)$. The symbols mean: $\square$ ($\sigma = 0.1$, $E = 10^{-4}$), $*$ ($\sigma = 0.1$, $E = 3.162 \times 10^{-5}$), $+$ ($\sigma = 0.1$, $E = 8.165 \times 10^{-6}$), $\blacksquare$ ($\sigma = 0.025$, $E = 10^{-5}$) and $\odot$ ($\sigma = 1$, $E = 3.162 \times 10^{-5}$).

Ra/Ra_c	$\overline{\langle\|\mathbf{F}_C\|\rangle_{\mathcal{V}}}$	$\overline{\langle\|\mathbf{F}_I\|\rangle_{\mathcal{V}}}$	$\overline{\langle\|\mathbf{F}_V\|\rangle_{\mathcal{V}}}$	$\overline{\langle\|\mathbf{F}_B\|\rangle_{\mathcal{V}}}$
$E = 10^{-4}$				
1.08	2.34×10^5	1.78×10^3	4.62×10^3	6.54×10^3
1.62	6.19×10^5	9.15×10^3	1.09×10^4	2.71×10^4
2.69	1.77×10^6	7.82×10^4	3.39×10^4	1.11×10^5
5.39	3.97×10^6	4.72×10^5	1.02×10^5	3.26×10^5
8.08	7.02×10^6	1.77×10^6	2.56×10^5	7.16×10^5
10.78	1.02×10^7	3.97×10^6	4.58×10^5	1.16×10^6
16.16	1.49×10^7	9.62×10^6	9.92×10^5	2.12×10^6
26.94	2.10×10^7	2.26×10^7	2.15×10^6	4.19×10^6
37.70	2.53×10^7	3.79×10^7	3.63×10^6	6.36×10^6
53.88	3.13×10^7	6.14×10^7	5.71×10^6	9.73×10^6
$E = 3.162 \times 10^{-5}$				
1.57	2.03×10^6	2.05×10^4	2.49×10^4	4.73×10^4
3.14	8.04×10^6	2.29×10^5	8.67×10^4	3.41×10^5
12.56	5.35×10^7	1.32×10^7	1.44×10^6	4.61×10^6
31.40	1.10×10^8	7.52×10^7	6.68×10^6	1.46×10^7
109.91	2.26×10^8	4.95×10^8	3.65×10^7	6.87×10^7
188.41	2.94×10^8	1.06×10^9	6.72×10^7	1.31×10^8

Table 5: Modulus of the mean volume-averaged forces $\overline{\langle\|\mathbf{F}_*\|\rangle_{\mathcal{V}}} = \frac{1}{\mathcal{V}}\int_{\mathcal{V}}\sqrt{F_r^2 + F_\theta^2 + F_\varphi^2}\,dv$ for several Ra/Ra_c, $\sigma = 0.1$ and Ekman numbers 10^{-4} and 3.162×10^{-5}. The symbol $*$ indicates the forces which appear in the momentum equation. $\mathbf{F}_C = -2E^{-1}\mathbf{k} \times \mathbf{v}$, $\mathbf{F}_I = -(\mathbf{v}\cdot\boldsymbol{\nabla})\mathbf{v}$, $\mathbf{F}_V = \nabla^2\mathbf{v}$ and $\mathbf{F}_B = \Theta\mathbf{r}$ are the Coriolis force, inertial (advective part), viscous and buoyancy forces, respectively.

the buoyancy, Coriolis and inertial forces. Thus, on the basis of Fig. 4, Table 5 and the results of these authors, in the present study the physical properties are also expressed as functions of Ra_Q^* defined as follows. If

$$Ra^* = RaE^2\sigma^{-1}, \qquad \text{and} \qquad (12)$$

$$Nu^* = (Nu - 1)E\sigma^{-1} \qquad (13)$$

are the modified Rayleigh and Nusselt numbers, respectively, which neither depend on the viscosity nor the thermal diffusivity, then

$$Ra_Q^* = Ra^*Nu^*. \qquad (14)$$

For geophysical applications it is more useful to analyze the dependence of the properties of the fluid with Ra_Q^* rather than with Ra^*, based on the temperature contrast ΔT, because the latter is more difficult to estimate.

The relation between Ra, defined in Eq. (5), with that defined by Christensen and Aubert (2006), Ra^{CA}, is $Ra = (1 - \eta)Ra^{CA}$. The same relation holds for Ra^* and Ra_Q^* since E, σ agree, and $(Ra^*)^{CA}/(Ra_c^*)^{CA} = Ra^*/Ra_c^*$. The definitions of Ro (see Table 12 in the Appendix) and Nu are also the same in both studies, then the comparison is straightforward. Although $Ra_{Q_T}^*$ is used in Christensen (2002), we have checked that this change does not affect significantly the scaling laws obtained in that study, since it focused on high Ra convection with $Nu \gg 1$. On the other hand, the definitions of Re and K are the same.

8

The numerical resolutions, and the type of azimuthal symmetry imposed to obtain the solutions are indicated in Table 6. By comparing these results with those found for pure thermal convection with stress-free boundary conditions, we have found smaller $\overline{Re}$, larger $\overline{Re_p}$ and very similar $\overline{Nu}$ at moderately high Ra^* and low σ. For instance, for $E = 10^{-4}$, $\sigma = 0.1$ and $Ra^*/Ra_c^* = 53.88$ we obtain $\overline{Re} = 2144.6$, $\overline{Re_p} = 1303.4$ and $\overline{Nu} = 5.77$, while by extrapolating the stress-free results for $\sigma = 1$ and $\sigma = 0.3$ at $Ra/Ra_c \sim 50$ to $\sigma = 0.1$ and assuming a power law dependence on σ, $\overline{Re} \sim 2300$, $\overline{Re_p} \sim 1070$ and $\overline{Nu} \sim 5.26$, are obtained. So although $\overline{Re}$ is a little higher with stress-free conditions due to the strong zonal flows, the volume-averaged poloidal velocity is larger in the non-slip case. The heat transport at $r = r_o$ is very similar, probably because in this range of Ra the thermal boundary layers affect small areas of the external surface, and in rotating systems the width of these layers decreases when Ra increases (see Julien et al. (2012)).

To check the validity of analyzing the results versus a diffusivity-free parameter at high Ra with non-slip boundary conditions, Table 7 shows, like in Stelzer and Jackson (2013), the power laws, $Y = a(Ra_Q^*)^b E^c$, with the respective errors for the mean Rossby number, $\overline{Ro}$, ratio of the kinetic energy density to the non-axisymmetric part, $\overline{K/K_{na}}$, poloidal Rossby number, $\overline{Ro_p}$, modified Nusselt number, $\overline{Nu^*}$, axisymmetric Rossby number, $\overline{Ro_a}$, and the zonal Rossby number $\langle \overline{v_\varphi} \rangle E$, computed at $\theta = 3\pi/8$, $r = r_i + (r_o - r_i)/7$ (see the Appendix for the definitions). The points considered are included in Table 6, and the fittings are done by taking the maximal number of points that gives the best potential law by minimizing the fitting error.

Any of the exponents of E obtained in the scalings is very small indicating the low explicit dependence on this parameter, and the errors of the fittings can be even larger than those computed by neglecting the E dependence (see below for comparison). In addition, to verify the existence of power laws independent of the thermal diffusivity we have included the solutions of $\sigma = 0.025$ and $E = 10^{-5}$, and $\sigma = 1$ and $E = 3.162 \times 10^{-4}$, one order of magnitude above and below $\sigma = 0.1$. In these two cases not enough points were available to do a fitting, but, as can be seen in Fig. 5, there is a clear tendency of the solutions to follow the fitted lines, which have been included in the figure. Notice also that the lower E the lower the value of Ra_Q^* for which the points reach the fitted line. Consequently, taking into account that the spatial truncation, imposed symmetries and the errors of the very large integrations can easily change the weak dependence on E and σ, and that these dependences are not clear, we have followed Christensen and Aubert (2006) and plotted the scalings of the parameters versus Ra_Q^* alone to facilitate the comparison with previous studies.

Figure 5a-f, which contains the same information as Fig. 7 from Christensen (2002), shows the dependence of the mean spatially-averaged physical properties of Table 7 as functions of Ra_Q^*, for the same solutions of Fig. 4. They are computed as before, i.e. by only taking the points which minimize the fitting errors. It seems that the curves of $\overline{Ro_a}$ and $-\langle \overline{v_\varphi} \rangle E$ tend to a maximum value, consequently in these cases (and as before) the region of saturation at high Ra_Q^* is also discarded. We proceed

Ra/Ra_c	$\overline{Re}$	$\overline{Re_p}$	K_t/K	$\overline{Nu}$	σ_{K_p}	N_r	L	m_d
			$E = 10^{-4}$					
1.08	15.7	8.7	0.69	1.005	≈ 0	32	54	1
1.62	41.3	19.1	0.78	1.02	0.27	32	54	1
2.69	117.5	49.1	0.83	1.10	0.039	32	54	1
5.39	259.9	106.4	0.83	1.27	0.21	32	54	1
8.08	465.3	200.6	0.81	1.64	0.22	40	64	2
10.78	678.2	311.9	0.79	2.10	0.17	50	84	2
16.16	983.6	495.4	0.75	2.84	0.16	50	84	2
26.94	1389.1	776.5	0.69	3.92	0.14	70	128	2
37.70	1686.4	993.3	0.65	4.74	0.12	70	128	2
53.88	2144.6	1303.4	0.63	5.77	0.085	80	160	2
			$E = 3.162 \times 10^{-5}$					
1.26	29.1	14.9	0.74	1.009	≈ 0	32	54	2
1.57	47.7	21.9	0.79	1.02	≈ 0	32	54	2
3.14	174.5	65.1	0.86	1.10	0.30	50	84	2
6.28	449.4	160.9	0.87	1.33	0.20	50	84	2
9.42	771.4	299.2	0.85	1.71	0.17	50	84	2
12.56	1104.0	446.5	0.84	2.21	0.20	50	84	2
15.70	1362.7	574.3	0.82	2.62	0.15	50	84	2
31.40	2214.8	1008.6	0.79	4.20	0.12	70	128	2
47.10	3052.1	1416.2	0.78	5.62	0.12	70	128	2
78.50	4053.6	2097.1	0.73	7.86	0.13	80	192	2
109.91	4628.2	2567.8	0.69	9.47	0.12	80	192	2
188.41	6140.5	3657.0	0.65	12.24	0.08	80	224	2
			$E = 8.165 \times 10^{-6}$					
1.21	32.	17.	0.74	1.006	≈ 0	50	84	4
2.77	251.	99.	0.84	1.12	0.40	50	84	4
5.28	605.	220.	0.87	1.29	0.31	70	128	4
10.41	1343.	496.	0.86	1.77	0.22	70	128	4
20.81	2664.	1065.	0.84	3.21	0.18	80	192	4
27.75	3330.	1348.	0.84	4.02	0.14	80	192	4
41.62	4379.	1819.	0.83	5.44	0.15	80	192	4
104.06	7647.	3228.	0.82	9.78	0.13	80	224	4
173.43	9999.	4527.	0.79	13.56	0.12	90	256	4
242.80	12111.	5780.	0.77	16.88	0.10	100	300	4

Table 6: Relative Rayleigh number Ra/Ra_c, mean Reynolds and poloidal Reynolds numbers, $\overline{Re}$ and $\overline{Re_p}$, mean ratio of the toroidal to the total KED, $\overline{K_t/K}$, mean Nusselt number, $\overline{Nu}$, relative variance of the poloidal KED, σ_{K_p}, numerical resolutions, N_r and L, and imposed m_d-fold azimuthal symmetry for three Ekman numbers. The Prandtl number is 0.1.

in this way because we are interested in obtaining the extrapolation at low Ra_Q^* (see Sec. 7). The validity of this extrapolation is based on Fig. 5, which shows the tendency of the curves to reach the power law (solid line) at lower values of Ra_Q^* when E is decreased. On the other hand, we have checked that the saturation is not a consequence of the enforced two-fold symmetry by redoing some points without the symmetry. This feature was also described in the experiments of Shew and Lathrop (2005) and Manneville and Olson (1996).

The power laws obtained correspond to low Rossby number convection for which the Coriolis force is still funda-

Y	a	$\epsilon(a)$	b	$\epsilon(b)$	c	$\epsilon(c)$
$\overline{Ro}$	1.28	0.10	0.35	0.0046	−0.0060	0.0094
$\overline{K/K_{na}}$	0.24	0.026	−0.22	0.013	−0.043	0.014
$\overline{Ro_p}$	1.23	0.18	0.42	0.0087	0.0092	0.018
$\overline{Nu^*}$	0.077	0.024	0.54	0.012	−0.015	0.033
$\overline{Ro_a}$	0.60	0.094	0.36	0.0079	−0.054	0.016
$\langle \overline{v_\varphi} \rangle E$	0.084	0.016	0.31	0.011	−0.059	0.019

Table 7: Coefficients and absolute errors of the power laws $Y = a(Ra_Q^*)^b E^c$, Y being the mean Rossby number, $\overline{Ro}$, ratio of the total to the non-axisymmetric KEDs, $\overline{K/K_{na}}$, poloidal Rossby number, $\overline{Ro_p}$, modified Nusselt number, $\overline{Nu^*}$, axisymmetric Rossby number, $\overline{Ro_a}$, and zonal Rossby number $\langle \overline{v_\varphi} \rangle E$. The Prandtl number is 0.1.

Y	a	$\epsilon(a)$	b	$\epsilon(b)$
$\overline{Ro}$	1.34	0.038	0.35	0.0034
$\overline{K/K_{na}}$	0.31	0.029	−0.24	0.014
$\overline{Ro_p}$	1.14	0.062	0.42	0.0064
$\overline{Nu^*}$	0.089	0.0092	0.54	0.010
$\overline{Ro_a}$	0.96	0.098	0.35	0.010
$\langle \overline{v_\varphi(r_{int})} \rangle E$	0.14	0.019	0.29	0.015
$\langle \overline{v_\varphi(r_{mid})} \rangle E$	0.15	0.015	0.35	0.010
$\langle \overline{v_\varphi(r_{out})} \rangle E$	0.15	0.014	0.42	0.010

Table 8: Coefficients and absolute errors of the power laws $Y = a(Ra_Q^*)^b$, with Y being the mean Rossby number, $\overline{Ro}$, ratio of the total to the non-axisymmetric KEDs, $\overline{K/K_{na}}$, poloidal Rossby number, $\overline{Ro_p}$, modified Nusselt number, $\overline{Nu^*}$, axisymmetric Rossby number, $\overline{Ro_a}$, and zonal Rossby number $\langle \overline{v_\varphi} \rangle E$ with $r_{int} = r_i + (r_o - r_i)/7$, $r_{mid} = r_i + (r_o - r_i)/2$ and $r_{out} = r_i + 6(r_o - r_i)/7$.

mental to understand the dynamics, because by taking into account Eqs. (12)-(14) and that $Ra_c \sim E^{-4/3}$ (see Dormy et al. (2004); Net et al. (2008, 2012), among others) $Ra_Q^* \sim (Ra/Ra_c)E^{5/3}(Nu - 1)\sigma^{-2}$, and for small but finite Ra_Q^*, when $E \to 0$, $(Ra/Ra_c)(Nu - 1)\sigma^{-2} \to \infty$. Since it is expected that $(Nu - 1)\sigma^{-2}$ remains bounded, Ra/Ra_c must tend to infinity.

The power laws, $Y = a(Ra_Q^*)^b$, with their statistical errors are shown in Table 8 and Eqs. (15-19) and (22). The first five equations are

$$\overline{Ro} = 1.34(Ra_Q^*)^{0.35}, \tag{15}$$

$$\overline{K/K_{na}} = 0.31(Ra_Q^*)^{-0.24}, \tag{16}$$

$$\overline{Ro_p} = 1.14(Ra_Q^*)^{0.42}, \tag{17}$$

$$\overline{Nu^*} = 0.089(Ra_Q^*)^{0.54}, \tag{18}$$

$$\overline{Ro_a} = 0.96(Ra_Q^*)^{0.35}. \tag{19}$$

The scaling of the Nusselt number agrees very well with that given by Christensen and Aubert (2006) for a thermal-driven dynamo with non-slip boundaries. Translated to our parameter they found

$$\overline{Nu^*} = 0.095(Ra_Q^*)^{0.53}, \tag{20}$$

Since at very high Ra the difference is very small, and in agreement with Soderlund et al. (2012), our results confirm that the

heat transport remains almost unperturbed under the presence of a magnetic field. In contrast that for $\overline{Ro}$,

$$\overline{Ro} = 1.01(Ra_Q^*)^{0.41} \tag{21}$$

does not match so well. Since the presence of a magnetic field almost does not change the modified Nusselt number, $\overline{Nu^*}$ and decreases $\overline{Ro}$, it might damp the zonal part of the velocity field.

As said before, Figs. 5e,f show that $\overline{Ro_a}$ and $-\langle \overline{v_\varphi} \rangle E$ seem to tend to constant values for sufficiently large Ra_Q^* and non-vanishing E, i.e. in the high Rossby number limit. As a consequence of this behavior there is a change in the sign of the slope of $\overline{K/K_{na}}$, already found by Christensen (2002) for stress-free boundary conditions. Beyond the maximum of $\overline{K/K_{na}}$, the regime of fully developed convection without equatorial symmetry and the highest heat transfer rates begin. For $E = 10^{-4}$, the maximum is close to $Ra_Q^* = 3 \times 10^{-4}$, namely it is about six times the critical.

Our scaling relations for the mean zonal flow given by Fig. 5f at $\theta = 3\pi/8$ are

$$-\langle \overline{v_\varphi} \rangle E = 0.14(Ra_Q^*)^{0.29} \text{ if } r = r_i + (r_o - r_i)/7, \tag{22}$$

with and error about 4% for the exponent and 9% for the prefactor. At other radial distances (not shown in the figure) we have found

$$-\langle \overline{v_\varphi} \rangle E = 0.15(Ra_Q^*)^{0.35} \text{ if } r = r_i + (r_o - r_i)/2, \quad \text{and} \tag{23}$$

$$\langle \overline{v_\varphi} \rangle E = 0.15(Ra_Q^*)^{0.42} \text{ if } r = r_i + 6(r_o - r_i)/7. \tag{24}$$

In agreement with the quasi-geostrophic theory of Gillet et al. (2007) the radial dependence of $\langle \overline{v_\varphi} \rangle$ on r is very strong. The mean zonal flow is negative everywhere, but close to the outer boundary. The Rossby number based on it ($Ro_{\langle \overline{v_\varphi} \rangle} = |\langle \overline{v_\varphi} \rangle|E$) is of the same order of magnitude at $Ra_Q^* = 10^{-2}$ for all r, but for lower Ra_Q^* it decreases outwards very fast. For instance at $Ra_Q^* = 10^{-15}$ it changes from 6.25×10^{-6} near the inner core to 8.44×10^{-7} at the center of the shell and to 7.5×10^{-8} near the external surface.

The Rossby number $Ro_{\langle \overline{v_\varphi} \rangle}$ at $r = r_i + (r_o - r_i)/7$ exhibits a different power law dependence than the mean axisymmetric Rossby number $\overline{Ro_a}$ given by Eq. (19). The ratio of the latter to the former decreases slowly from 5 at $Ra_Q^* = 10^{-2}$ to 1 at $Ra_Q^* = 10^{-15}$, meaning that at very low Ra_Q^*, the contribution of the axisymmetric poloidal (radial and colatitudinal) component of the velocity field becomes smaller. In fact the axisymmetric poloidal component is, at least, 89% smaller than the toroidal (see Table 2).

The flow patterns of the solutions computed before ($Ra = 10^6$) and after ($Ra = 2 \times 10^6$) the maximum of $\overline{K/K_{na}}$, i.e., near $Ra_Q^* = 3 \times 10^{-4}$ in Fig. 5 are shown in Figs. 6 and 7. The first shows, from top to bottom, a sequence of six snapshots taken at times $t = 0$, $t = 0.0002$, $t = 0.0004$, $t = 0.0006$, $t = 0.0008$ and $t = 0.001$. Three projections of the deviation of the temperature with respect to its average on a surface of the same radius, i.e. $T(r, \theta, \varphi, t) - \langle T \rangle_S(r, t)$, are displayed in the left group of plots. The radius of the spherical surfaces is $r = r_i + 0.275d$, although they are represented with the same size as the other sections. It
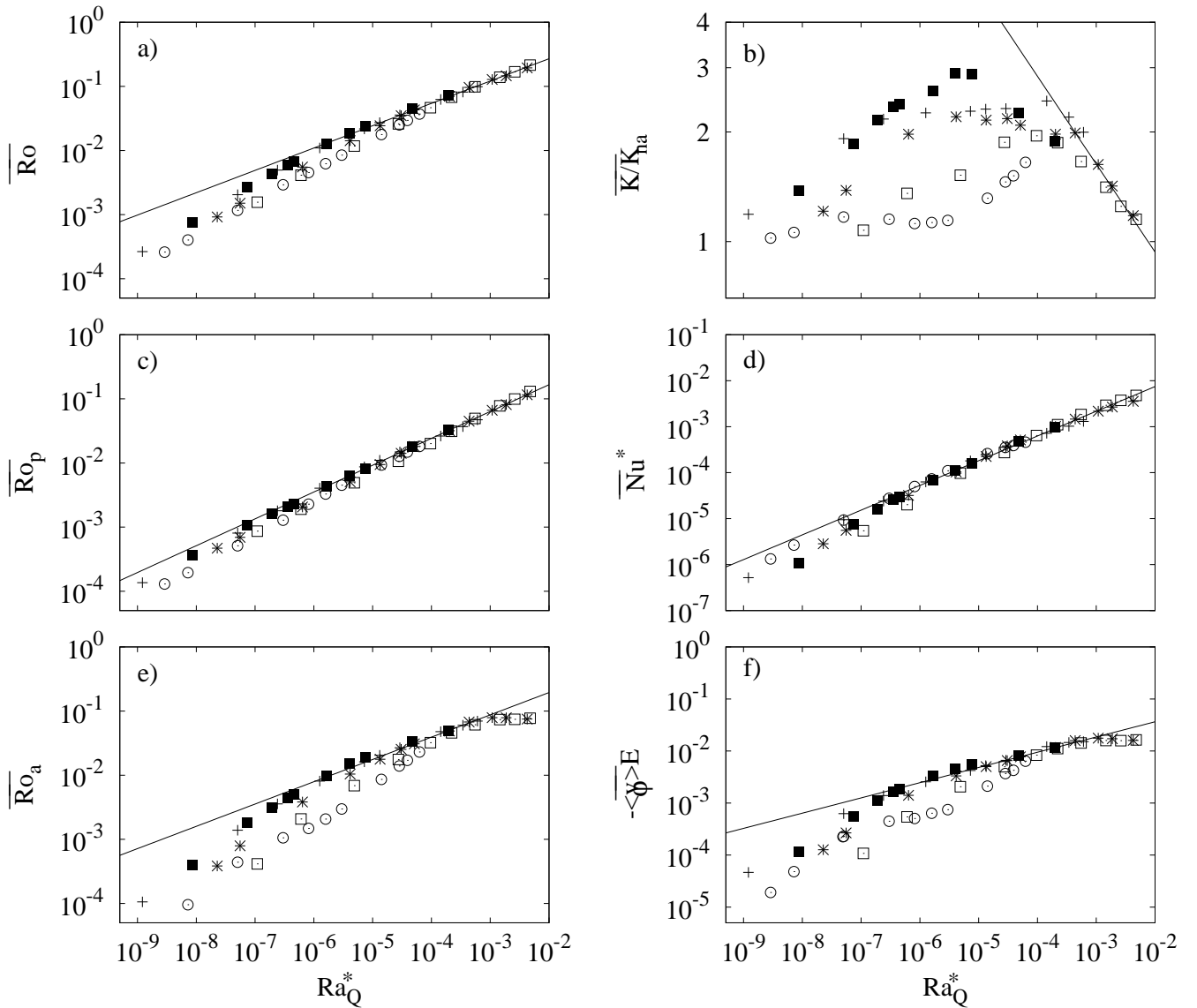
Figure 5: Mean (a) Rossby number, $\overline{Ro}$, (b) ratio of the total to the non-axisymmetric KEDs, $\overline{K/K_{na}}$, (c) poloidal Rossby number, $\overline{Ro_p}$, (d) modified Nusselt number, $\overline{Nu^*}$, (e) axisymmetric Rossby number, $\overline{Ro_a}$, and (f) scaled mean zonal flow, $-\overline{\langle v_\varphi \rangle}E$, versus the flux-based Rayleigh number, Ra_Q^*. The symbols mean: $\square$ ($\sigma = 0.1$, $E = 10^{-4}$), $*$ ($\sigma = 0.1$, $E = 3.162 \times 10^{-5}$), $+$ ($\sigma = 0.1$, $E = 8.165 \times 10^{-6}$), $\blacksquare$ ($\sigma = 0.025$, $E = 10^{-5}$) and $\odot$ ($\sigma = 1$, $E = 3.162 \times 10^{-5}$). The laws corresponding to the solid lines are in Table 8.

corresponds approximately to the radius where the temperature perturbation is maximum. The middle projections are taken on the equatorial plane, and the right ones on a meridional section through $\varphi = 0$. The scale of greys (colors online) is the same for all the contour plots corresponding to each solution, with white (red) meaning hot fluid. The same projections are taken for the kinetic energy density (right group of plots), but with the spherical projections taken close to the outer boundary at $r = r_i + 0.975d$ with a polar point of view. In these contour plots the time intervals are selected to see the breakings and mergings of the cells and vortices.

Despite the complex time dependence of the solution of Fig. 6, the contour plots retain remainders of regular patterns. The z-dependence of the flow shown in the meridional sections

is weak, and the flow is symmetric with respect to the equatorial plane. The polar convection starts to be noticeable (see the spherical sections in the left column of Fig. 6). Another remarkable feature of the contour plots of $T - \langle T \rangle_S$ is that the cells of convection tend to increase their radial and azimuthal extension when Ra increases, in agreement with the results of Tilgner and Busse (1997) and Aubert et al. (2001). As a consequence a double-layered pattern is formed. On the other hand, a two cylindrical layer structure with spiraling vortices can also be discovered in the contour plots of $|\mathbf{v}|^2$. By observing the vortices of the spherical and equatorial sections in the right column of Fig. 6 (but easily with the help of a movie) one can see that the maximum of $|\mathbf{v}|^2$ moves from the equatorial inner (first row, equatorial plot) to the nearly polar outer boundary (fourth row,
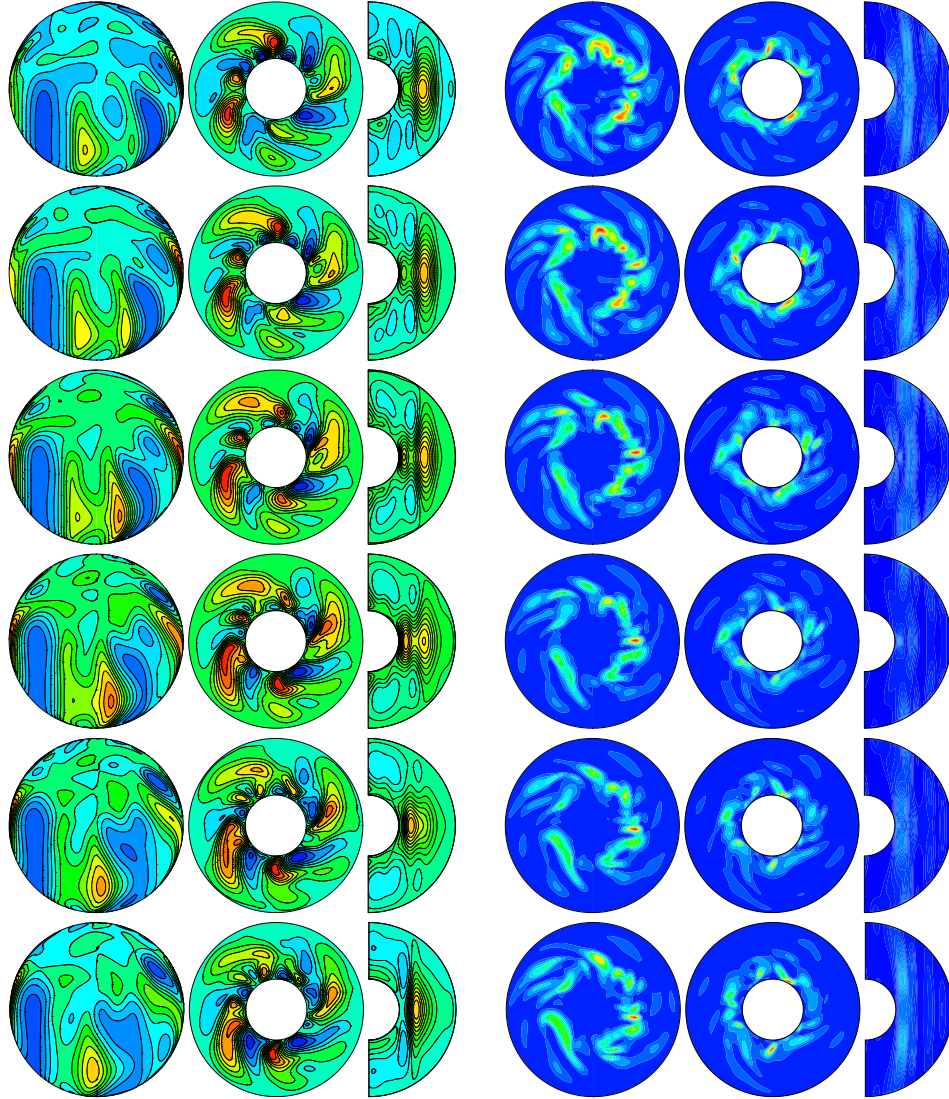
Figure 6: At left, contours of the deviation of the temperature from its average, $T(r_f, \theta, \varphi, t) - \langle T \rangle_S(r, t)$, on a spherical surface, the equatorial plane and a meridional section for six snapshots corresponding to the evolution of a spatio-temporal chaotic solution, and at right contour plots of the kinetic energy density, on polar, equatorial and meridional projections. From top to bottom, the snapshots are taken at $t = 0$, $t = 0.0002$, $t = 0.0004$, $t = 0.0006$, $t = 0.0008$ and $t = 0.001$. The Rayleigh number is $Ra = 10^6$ before the maximum of $\overline{K/K_{na}}$.

polar plot) along a column.

The spherical sections for $T - \langle T \rangle_S$ in Fig. 7 are taken at $r = r_i + 0.3625d$, and those for $|\mathbf{v}|^2$ at $r = r_i + 0.9625d$. As can be observed in the meridional sections, the equatorial symmetry is broken, and the z-dependence of the flow is enhanced, although a rough quasi-geostrophic structure still remains. In this case one can observe hot plumes towards the outer boundary, their expansion in the direction of rotation and progressive cooling, while new cells are emerging at the hot boundary. When the plumes rise and expand spiralling in the prograde direction they can reconnect with others at larger longitudes forming a shell of hotter fluid in the external part. The boundary of the two regions is located around $r \approx r_i + d/3$. On the other hand, the convection in the polar regions is now clearly developed as can be perceived in the contour plots of $|\mathbf{v}|^2$, as well as in those of $T - \langle T \rangle_S$ on the spherical projections.

6. Comparison with previous experimental results

In this section the numerical fittings of the time-averaged quantities will be compared with the scalings obtained in previous experimental and numerical studies with water (Aubert et al. (2001)), liquid gallium (Aubert et al. (2001); Gillet et al. (2007)) and liquid sodium (Shew and Lathrop (2005)), and setups of radius ratio near 0.35. In each case we adopt estimators close to those used in each work.

6.1. Aubert et al. (2001)

The Ekman number used in Aubert et al. (2001) falls in the range $10^{-7} < E < 10^{-6}$. Although it is up to two orders of magnitude smaller than ours, and their $\sigma = 7$ and 0.023 differ in one order, significant similarities are found, some of them already commented in the preceding sections. To quantify the intensity of the flows, Aubert et al. (2001) measured local quantities.
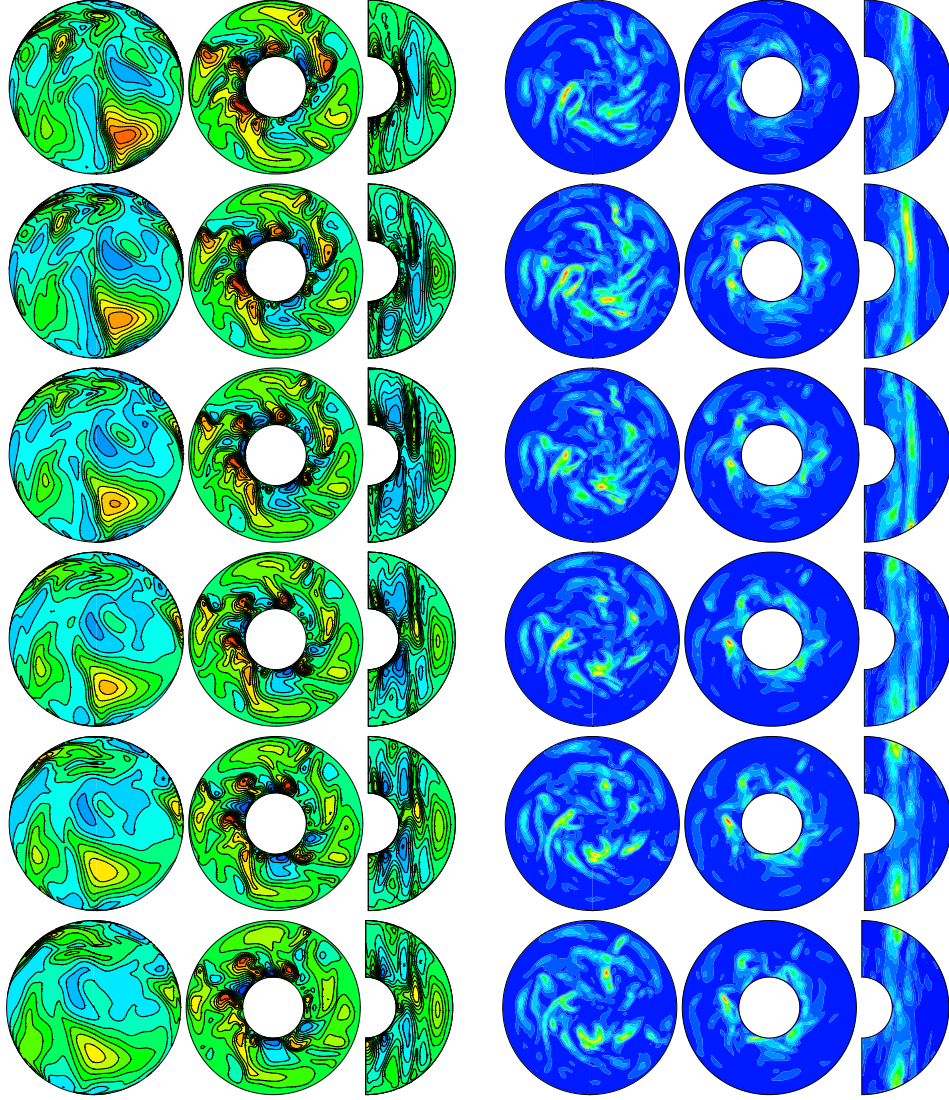
Figure 7: Same contour plots as in Fig. 6. From top to bottom, the snapshots are taken at $t = 0$, $t = 0.0001$, $t = 0.0002$, $t = 0.0003$, $t = 0.0004$, and $t = 0.0005$. The Rayleigh number is $Ra = 2 \times 10^6$ after the maximum of $\overline{K/K_{na}}$.

For the convective part they employed the absolute variance of the radial component of the velocity field $\tilde{\sigma}_{v_r} = \sqrt{\overline{(v_r - \overline{v_r})^2}}$ at the radial distance $r = r_{\max}$ where $\tilde{\sigma}_{v_r}$ is maximal, which falls near the inner boundary. As zonal flow they measured a time-average of the longitudinal component $\overline{v_\varphi}$ of $\mathbf{v}$. On the other hand, our dimensionless parameters, as well as time and length scales, are the same as those of them, so the comparison is straightforward.

All the flow patterns described in Aubert et al. (2001) for the liquid gallium are turbulent, even at $Ra = 1.2Ra_c$. This contrast with our results in which periodic and quasiperiodic motions appear near the onset of convection even with $\sigma = 0.025$. The discrepancy is probably due to the experimental set-up that was not well suited for measurements of flows near the onset, so it was difficult to find experimentally periodic motions in the low range of parameters.

The set of scaling laws derived in Cardin and Olson (1994),

under the assumption of quasi-geostrophic flow and negligible dissipation in the outer Ekman layer, were adopted in Aubert et al. (2001) when the inertial terms dominate the dynamics, i.e. when $Ra_{Q_T}E^{3/2}\sigma^{-2} > 1$, $Ra_{Q_T} = Ra\overline{Nu}$ being the Rayleigh number based on the total heat flux. In order to validate that this condition is fulfilled in our calculations, the product is plotted versus $Ra/Ra_c - 1$ in Fig. 8a for $E = 10^{-4}$, $E = 3.162 \times 10^{-5}$, and $E = 8.165 \times 10^{-6}$ and $\sigma = 0.1$. For any of the solutions plotted the values are larger than 10, so the inertial terms play a significant role.

In the experiments with gallium they obtained an asymptotic law for the Rossby number $Ro_{\tilde{\sigma}_{v_r}} = \tilde{\sigma}_{v_r}E$, based on the r.m.s. radial velocity, $Ro_{\tilde{\sigma}_{v_r}} \sim (Ra_{Q_T}^*)^{2/5}$, which agrees with our numerical results for $\overline{Ro_p}$ (see Eq. (17)), although the latter is volume-averaged and computed with the advected heat flux. Moreover, in Fig. 8b, $-\langle\overline{v_\varphi}\rangle$, computed near the inner boundary and close to the equator (see figure caption), is shown ver-
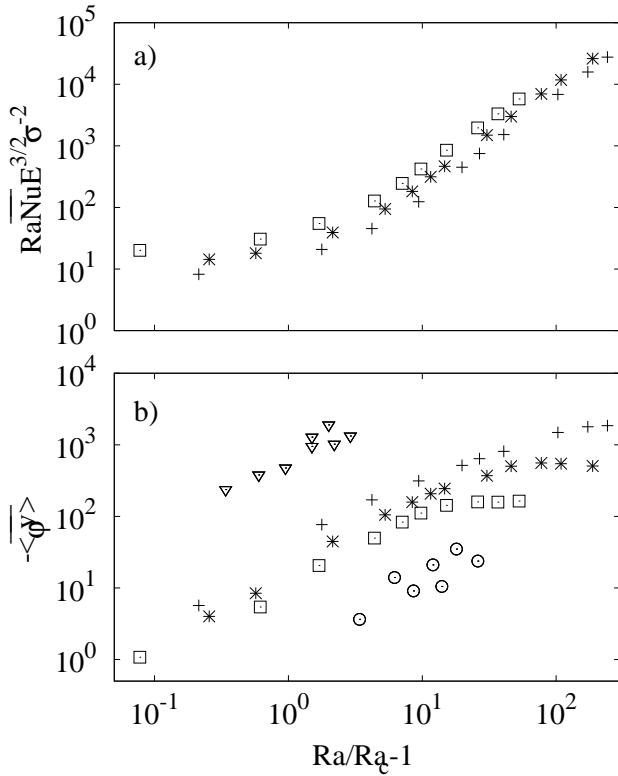
13

Figure 9: Mean axisymmetric toroidal Reynolds number, $\overline{Re_t^a}$, plotted versus the mean poloidal Reynolds number, $\overline{Re_p}$. The symbols stand for: (□) $E = 10^{-4}$, (∗) $E = 3.162 \times 10^{-5}$, and + $E = 8.165 \times 10^{-6}$, and $\sigma = 0.1$.

Figure 8: (a) The flux-based Rayleigh number, $Ra\overline{Nu}$, normalized with $E^{3/2}\sigma^{-2}$, and (b) time average of the azimuthally-averaged azimuthal component of the velocity field, $-\langle\overline{v_\varphi}\rangle$, at $r = r_i + (r_o - r_i)/7$ and $\theta = 3\pi/8$, both plotted versus $Ra_c/Ra - 1$. The symbols mean: (□) $E = 10^{-4}$, (∗) $E = 3.162 \times 10^{-5}$, and (+) $E = 8.165 \times 10^{-6}$. The Prandtl number is $\sigma = 0.1$. Moreover, (▽) and (⊙) correspond to experimental measures in liquid gallium and water, respectively, taken from Aubert et al. (2001).

sus $Ra/Ra_c - 1$. To facilitate the comparison, the dimensional measures of $-\overline{v_\varphi}^d$ with gallium for $E = 1.5 \times 10^{-6}$ and water for $E = 2.4 \times 10^{-6}$, extracted from Aubert et al. (2001), are non-dimensionalized and superposed in the same figure. They were taken at the equator and near the inner boundary. In spite of dealing with global and local quantities for different E, the order of magnitude of $-\langle\overline{v_\varphi}\rangle$ and $-\overline{v_\varphi}$ and the tendency of the curves are coherent. Our curves fall between those experimental, reflecting the intermediate σ value, and the relatively high E for which they were computed. On the other hand, as it has been shown in Sec. 5, for each decreasing E there is an increasing Ra from which $-\langle\overline{v_\varphi}\rangle$ remains constant. When $E \to 0$ the saturation of the solutions could be delayed to $Ra \to \infty$.

6.2. Gillet et al. (2007)

In Gillet et al. (2007) the relation between the volumetric r.m.s radial velocity and mean zonal flows, defined as

$$\tilde{U} = \left[\frac{1}{\mathcal{V}}\int_{\mathcal{V}}(\tilde{\sigma}_{v_r})^2\,dv\right]^{1/2} \quad \text{and} \quad \hat{U} = \left[\frac{1}{\mathcal{V}}\int_{\mathcal{V}}(\overline{v_\varphi})^2\,dv\right]^{1/2},$$

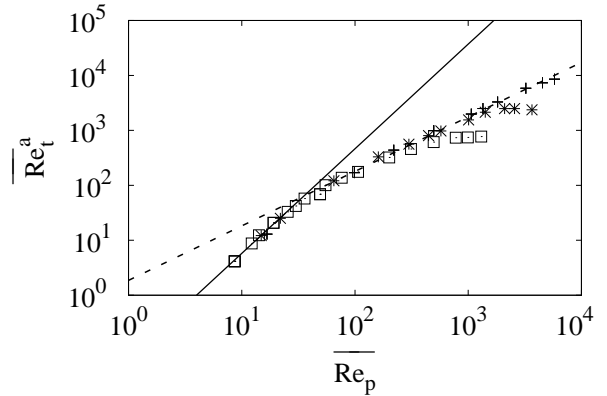respectively, was analyzed experimentally and checked with a quasi-geostrophic model. The experimental apparatus was composed by and external sphere, but the internal boundary was a cylinder, so probably it favoured the appearence of quasi-geostrophic flows. To compare with their results the zonal motions will be quantified by using the mean axisymmetric toroidal Reynolds number, $\overline{Re_t^a}$, defined in Table 12 because our $\langle\overline{v_\varphi}\rangle$ is only spatially averaged in longitude. The convective motions are estimated with the mean poloidal Reynolds number $\overline{Re_p}$ because it is the closest volumetric quantity we have monitored.

The results are shown in Fig. 9, for the three Ekman numbers considered and $\sigma = 0.1$. Three different regimes can be identified. At weak supercritical conditions, $\overline{Re_p} \in [1, 30]$, the dependence (shown by the solid line) is nearly quadratic, i.e. $\overline{Re_t^a} = 0.05(\overline{Re_p})^{1.96}$, within a 7% error in the exponent and 50% in the prefactor, in agreement with Gillet et al. (2007). For values $\overline{Re_p} > 30$ we have obtained $\overline{Re_t^a} = 1.86\overline{Re_p}^{0.99}$ (dashed line), within a 3% error in the exponent, and 16% in the prefactor. The zonal contribution starts to be important in the solutions belonging to this range, and thus the ratio $\overline{K/K_{na}}$ of Fig. 5 reaches the highest constant value and starts to decrease. At sufficiently high $\overline{Re_p}$, $\overline{Re_t^a}$ saturates as $\langle\overline{v_\varphi}\rangle$ does.

This behavior differs from that described in Gillet et al. (2007) for $\hat{U}$ versus $\tilde{U}$. They only found two σ-independent regimes, at the lowest Re, $\hat{U} \sim \tilde{U}^2$, and $\hat{U} \sim \tilde{U}^{4/3}$ at the highest, which corresponds to our intermediate case $\overline{Re_t^a} = 2\overline{Re_p}$. The difference between the powers 1 and 4/3 is in part due to the quasi-geostrophic model, but also to the different estimators used. For instance $\overline{Re_t^a}$ does not include the non-axisymmetric poloidal component of v_φ, and the poloidal component of the velocity field contains contributions of v_θ and v_φ. The main difference is that our almost linear relation breaks down when the equatorial symmetry of the solutions is lost, i.e. when the slope of the ratio $\overline{K/K_{na}}$ becomes negative (see Fig. 5b). Consequently, this saturation cannot be present in the two-dimensional quasi-geostrophic simulations of Gillet et al. (2007).

Figure 9 also allows to compare the strength of the zonal flow versus that of the convective vortices with non-slip boundary
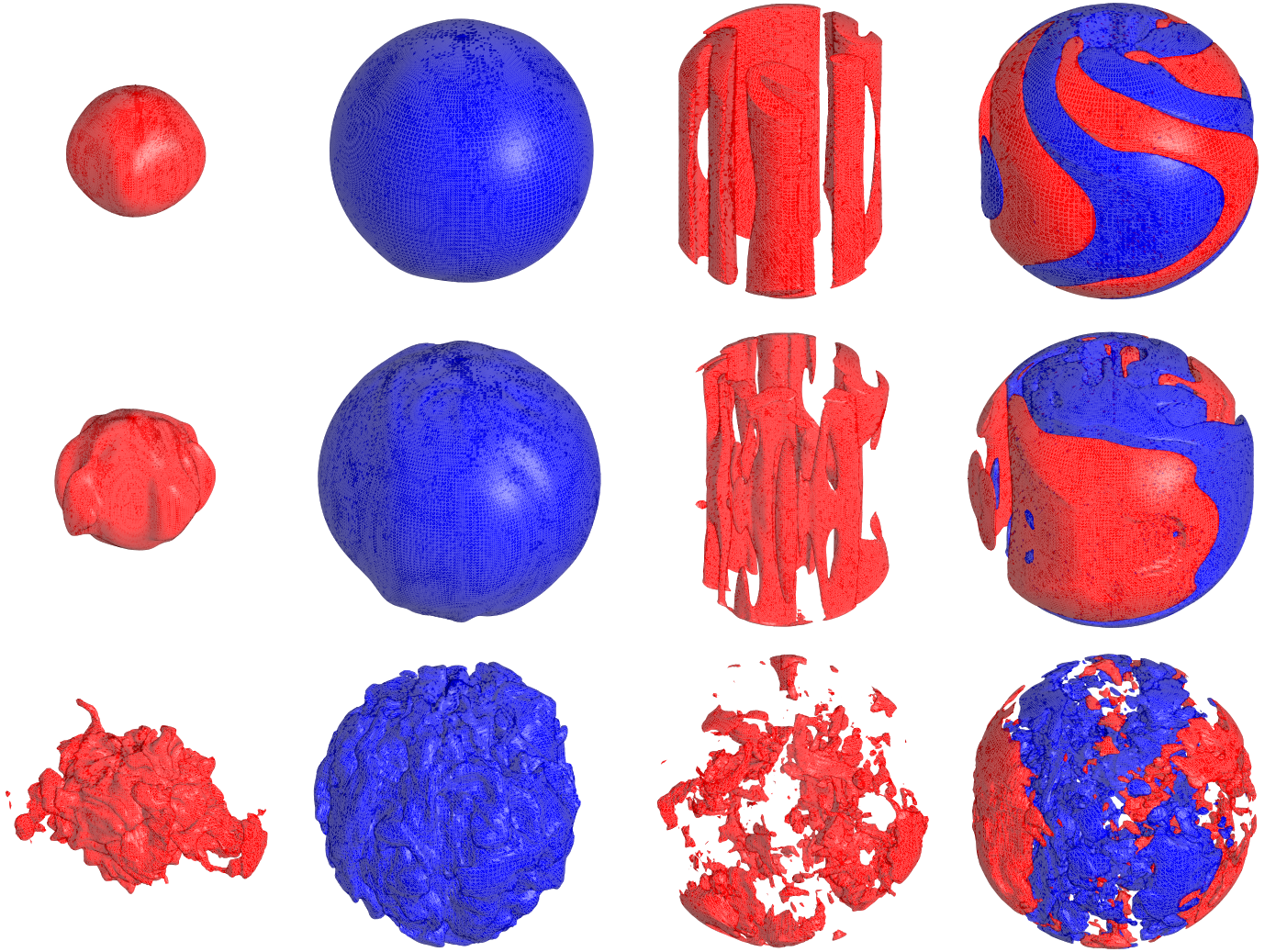
Figure 10: From left to right snapshots of the isosurfaces of T (hot and cold respectively), $|\mathbf{v}|^2$, and v_φ. From top to bottom, the Rayleigh numbers are $Ra = 3.43 \times 10^5$, $Ra = 10^6$ and $Ra = 10^7$, and $E = 10^{-4}$, $\sigma = 0.1$.

conditions and that found by Christensen (2002) with stress-free boundaries, $\sigma = 1$ and $E = 10^{-4}$. At low Ra the convective vortices dominate over the mean zonal flow, as was already seen in Fig. 5 in the ratio $\overline{K/K_{na}}$ in agreement with the preceding study. When $\overline{Re_p} > 30$ the slopes also match very well, although with a small prefactor in the case of the non-slip conditions.

The change of slope from weak to high supercritical regimes, as was mentioned in Sec. 1, was attributed in Christensen (2002) to a decorrelation of the Reynolds stresses due to a gradual loss of geostrophy. However, it was also observed in the quasi-geostrophic model of Gillet et al. (2007). According to these authors, this happens because the mean zonal flow surpasses the non-zonal convection as a consequence of the increase of the characteristic length scale of the convection. Our results confirm the breakdown of geostrophy, and show that at very high Ra/Ra_c and $E \rightarrow 0$ the mean zonal flow and the convective velocity differ by a factor, i.e. the Rhines theory applied

in Gillet et al. (2007), which gives a larger exponent, is scarcely fulfilled.

Characteristic solutions for three states found are shown in Fig. 10. The snapshots of the isosurfaces of the temperature $T = T_c + \Theta$, $|\mathbf{v}|^2$, and v_φ are plotted for the parameters indicated in the figure caption. At $Ra = 3.43 \times 10^5$ the solution is representative of flows in the first stage. The isosurfaces of $T \in [1.8 \times 10^6, 5.3 \times 10^6]$, taken at $T = 4.1 \times 10^6$ and $T = 2 \times 10^6$, those of $|\mathbf{v}|^2 \in [1.9 \times 10^{-11}, 2.7 \times 10^4]$ at $|\mathbf{v}|^2 = 4.5 \times 10^3$, and those of $v_\varphi \in [-1.5 \times 10^2, 1.2 \times 10^2]$ at $|v_\varphi| = 5$, resemble very much the eigenfunctions of the linear problem. In the second row $Ra = 10^6$. The isosurfaces of $T \in [5.4 \times 10^6, 1.5 \times 10^7]$ correspond to $T = 1.1 \times 10^7$ and $T = 5.8 \times 10^6$, those of $|\mathbf{v}|^2 \in [2.8 \times 10^{-10}, 1.3 \times 10^6]$ to $|\mathbf{v}|^2 = 1.5 \times 10^5$, and those of $v_\varphi \in [-1.1 \times 10^3, 5.9 \times 10^2]$ to $|v_\varphi| = 1.1 \times 10^2$. As can be seen, in the second region the zonal flow gains intensity, and the advection of the temperature deforms their isosurfaces, but the non-vanishing veloc-

15

ity field remains concentrated in a cylindrical shell. Then the quasi-geostrophic approximation can still capture mean properties of the flow. The figures in the third row are plotted for $Ra = 10^7$, which belong to the zone of saturation. The isosurfaces of $T \in [5.3 \times 10^7, 1.5 \times 10^8]$ are taken at $T = 8.8 \times 10^7$ and $T = 6.5 \times 10^7$, those of $|\mathbf{v}|^2 \in [3.5 \times 10^{-3}, 5.1 \times 10^7]$ at $|\mathbf{v}|^2 = 1.2 \times 10^7$, and those of $v_\varphi \in [-7.1 \times 10^3, 5.2 \times 10^3]$ at $|v_\varphi| = 1.7 \times 10^3$. Now the reflectional symmetry of the solutions with respect to the equator is broken and strong turbulent convection fills the spherical shell. Although the mean zonal flow maintains its strength, its ratio to the convective part has decreased (see Fig. 5).

6.3. Shew and Lathrop (2005)

Figure 11 contains several curves computed in order to compare with the experimental results of Shew and Lathrop (2005) with liquid sodium ($\sigma = 0.010$) in a set-up similar to that used in Aubert et al. (2001) but with a slim rotation axis and an internal sphere, which breaks the cylindrical configuration. For the comparison $E^S = E/2$ and $Ra^S \equiv Ra$ will be taken into account, the super-index S meaning values used in Shew and Lathrop (2005). In the definition of the Rayleigh number their centrifugal acceleration ($\Omega^2 \mathbf{r}$) plays the role of our gravity acceleration ($\gamma \mathbf{r}$).

Small scale convective, as well as large scale zonal flows, were observed in Shew and Lathrop (2005). The latter being determined from the time average of the azimuthal velocity, $(\overline{v_\varphi})^d$ (in m/s), collected from temperature probes situated close to the inner surface near the equator. They found retrograde mean zonal flows fulfilling the relation $(|\overline{v_\varphi}|)^d = (7\kappa/d)Ra^S E^S$, already mentioned in the introduction. In viscous units it gives $|\overline{v_\varphi}| = 350 Ra^S E$ for $\sigma = 0.010$. Notice that an additional factor (2) must multiply their dimensional Eq. (8)[1].

As it is well know (Tilgner and Busse (1997), Aubert et al. (2001), among many others) low σ fluids do not transfer heat efficiently. In the experiments with liquid sodium the Nusselt number never exceeded 2. Following Grossmann and Lohse (2000) and Shraiman and Siggia (1990), they derived the scaling relation $(Nu - 1)Ra^S\sigma^{-2} \sim (Re^S)^2(E^S)^{-1/3}$ by taking the thickness of the laminar boundary layer, $E^{1/3}d$, as length scale and balancing the global and the local energy dissipation of the convective cells. They found a very good agreement between the theory and the experimental data by estimating the convective velocity as the final velocity acquired by a parcel of fluid moving a distance d into a neighborhood of different temperature. In our case, with the larger $\sigma = 0.1$, $\overline{Nu}$ is already lower than 14 (see Table 6), and very similar to that found by Christensen (2002) for $\sigma = 0.3$ and stress-free boundary conditions. In order to find out if Prandtl numbers $O(10^{-1})$ fulfill the above scaling, Fig. 11a shows $(\overline{Nu}-1)Ra\sigma^{-2}$ plotted versus the global $\overline{Re_p}^2 E^{-1/3}$ for $\sigma = 0.1$. The numerical power law of the solid line gives

$$(\overline{Nu} - 1)Ra\sigma^{-2} = 218(\overline{Re_p}^2 E^{-1/3})^{0.98}, \qquad (25)$$
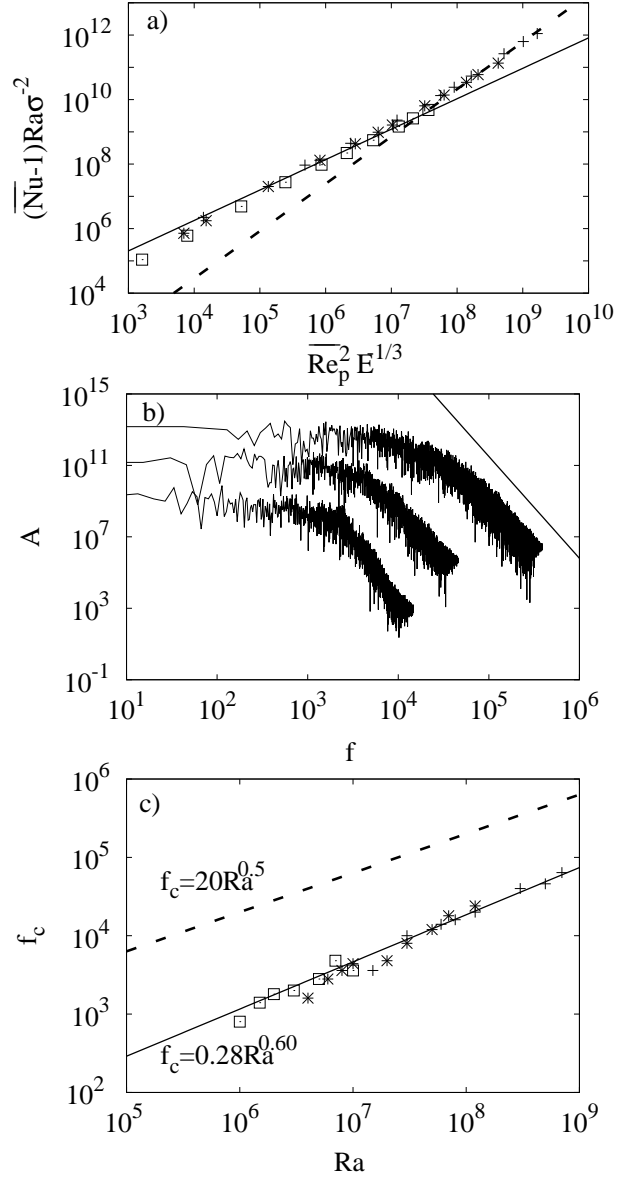
---

[1]Private communication from the authors

Figure 11: (a) Convective heat flux $(\overline{Nu} - 1)Ra\sigma^{-2}$ plotted versus $\overline{Re_p}^2 E^{-1/3}$. (b) Frequency spectra of the temperature perturbation for $E = 3.162 \times 10^{-5}$. They correspond from bottom to top to $Ra = 4 \times 10^6$, $Ra = 8 \times 10^6$ and $Ra = 5 \times 10^7$, respectively, and $\sigma = 0.1$. (c) Knee frequency f_c plotted versus Ra. The Prandtl number is 0.1. The symbols mean: ($\square$) $E = 10^{-4}$, ($*$) $E = 3.162 \times 10^{-5}$, and ($+$) $E = 8.165 \times 10^{-6}$. The solid line is our fitting, and the dashed that of Shew and Lathrop (2005) with $\sigma = 0.010$

with a 9% error in the exponent and 40% in the prefactor, agreeing with the experiment at small and moderate $\overline{Re_p}$, but a tendency to a larger tilt at high $\overline{Re_p}E^{-1/3}$ is found when E decreases. The new relation estimated from the dashed line is

$$(\overline{Nu} - 1)Ra\sigma^{-2} = 0.038 \times 10^{-2}(\overline{Re_p}^2 E^{-1/3})^{1.47}, \qquad (26)$$

with a 6% error in the exponent and 20% in the prefactor. Beside σ, a first source to explain this difference could be the possible dependence of the heat transfer on the latitude observed by Shew and Lathrop (2005). In addition, our convective heat

transfer is computed over the whole outer boundary, including the polar regions, where convection is strongly developed at high $\overline{Re_p}$ and the design of the apparatus prevents the development of convection there.

As in Aubert et al. (2001), periodic or quasiperiodic motions were not found in the sodium experiments. Shew and Lathrop (2005) obtained always non-periodic frequency spectra from the time series of the temperature taken also close to the inner boundary and the equator. These spectra present a sharp change of slope at the critical frequency, f_c, which according to them is $f_c^d = 2.0\Omega(\alpha\Delta T)^{1/2}$ Hz (knee frequency). The same behavior has been observed in Schmitt et al. (2008) and Figueroa et al. (2013) for the components of the magnetic field in experiments of spherical Couette flow under a dipolar magnetic field generated by magnets placed inside the inner sphere. In Fig. 11b three frequency spectra for the temperature perturbation Θ are shown. From bottom to top, they correspond to $Ra = 4 \times 10^6$, $Ra = 8 \times 10^6$ and $Ra = 5 \times 10^7$, and the same $E = 3.162 \times 10^{-5}$. In this case, a softer change of slope towards the high frequencies, but also close to -5.7 (marked by the solid line), can be recognized. In Fig. 11c f_c is plotted versus Ra for the non-periodic solutions. The points at $\theta = 3\pi/8$ fit to

$$f_c = 0.28Ra^{0.6} \quad \text{if} \quad r = r_i + (r_o - r_i)/7, \qquad (27)$$

represented by the solid line. The exponent error is 4% and 40% that of the prefactor. These large errors come from the uncertainty in determining f_c from Fig. 11b. Taking into account the error propagation, the application of this law can lead to errors larger than 100%.

We have found some variation of f_c with the radial distance for these turbulent flows, part of which could perhaps be due to the above mentioned errors. In

$$f_c = 0.39Ra^{0.57} \quad \text{if} \quad r = r_i + (r_o - r_i)/2 \quad \text{and} \qquad (28)$$
$$f_c = 2.5Ra^{0.45} \quad \text{if} \quad r = r_i + 6(r_o - r_i)/7, \qquad (29)$$

the exponents are obtained with errors of 3% and 6%, respectively, but those of the prefactor reach 30% and 50%.

The knee frequency of Shew and Lathrop (2005) can be rewritten in non-dimensional form as $f_c = 2(\sigma^{-1}Ra)^{1/2}$ when viscous units are used. With σ taken from the experiment, f_c gives

$$f_c = 20\sqrt{Ra}. \qquad (30)$$

This fitting is included in Fig. 11c. In the range of parameters studied it is approximately one order of magnitude higher.

As can be seen from the results included in Table 9 and Figs. 6 and 7, it seems that the equatorial symmetry breaking of the flow and the fully developed convection at very high latitudes can be related with the existence of the knee frequency in the spectrum. The sharp change of slope appears for Ra very close to the breaking, independently of E. 'Critical' Rayleigh numbers, Ra_{esb}, for the loss of symmetry in the intervals $[10^6, 1.5 \times 10^6]$ for $E = 10^{-4}$, $[4 \times 10^6, 6 \times 10^6]$ for $E = 3.162 \times 10^{-5}$, and $[1.5 \times 10^7, 3 \times 10^7]$ for $E = 8.165 \times 10^{-6}$ were found.

E	Ra/Ra_c	f_c	S_θ
	1.08	–	1
	1.62	–	1
	2.69	–	1
	5.39	800	1
10^{-4}	8.08	1400	0
	10.78	1800	0
	16.16	2000	0
	26.94	2800	0
	37.70	4800	0
	53.88	3600	0
	1.26	–	1
	1.57	–	1
	3.14	–	1
	6.28	1600	1
3.162×10^{-5}	9.42	2800	0
	12.56	3600	0
	15.70	4400	0
	31.40	4800	0
	78.50	12000	0
	109.91	18000	0
	188.41	24000	0
	1.21	–	1
	2.77	–	1
	5.28	3600	1
8.165×10^{-6}	10.41	10000	0
	20.81	12000	0
	27.75	14000	0
	41.62	18000	0
	104.06	40000	0
	173.43	46000	0
	242.80	64000	0

Table 9: Ekman number, relative Rayleigh number, Ra/Ra_c, approximate knee frequency, f_c, and equatorial symmetry, S_θ (1 with and 0 without symmetry) for $\sigma = 0.1$.

7. Estimations for the Earth's outer core

In this section, some of the scalings obtained in Secs. 5 and 6 are used to extrapolate some physical magnitudes for the Earth's outer core. Following Aubert et al. (2001) the flux-based Rayleigh number Ra_Q is obtained from the total heat rate at the core-mantle boundary (CMB), $\dot{Q}$, that according to Gubbins (2001) falls in the range $[1, 10]$ TW. However, recent estimations of Pozzo et al. (2012), based on new increased values of the thermal conductivity and considering several heat sources, give $\dot{Q} \approx 15$ TW. By taking $\dot{Q} = 10$ TW, the physical coefficients given in Table 10, the radial width of the Earth's outer core $d = 2.3 \times 10^6$ m, the Earth's radius at the CMB $r_{CMB} = 3.5 \times 10^6$ m, the radius at the internal core boundary $r_{ICB} = 1.2 \times 10^6$ m and $\gamma = 1.54 \times 10^{-6}$ s^{-2}, the non-dimensional parameter

$$Ra_{Q_T} = \frac{\alpha g(r_{CMB})\dot{Q}d^5}{4\pi r_{ICB}r_{CMB}^2 k\kappa\nu},$$

17

Property	GSN13	A-M01	SL05	CA06
Q (TW)	10	10	–	2
ν (m²/s)	10^{-6}	7×10^{-6}	10^{-6}	2×10^{-6}
κ (m²/s)	8.6×10^{-6}	4×10^{-6}	5×10^{-6}	8×10^{-6}
α (K⁻¹)	1.3×10^{-5}	–	–	10^{-5}
k (W/K m)	100	–	–	–
d (m)	2.3×10^{6}	2.3×10^{6}	2×10^{6}	2.3×10^{6}
E	2.6×10^{-15}	10^{-14}	10^{-15}	5×10^{-15}
σ	0.1	1	0.2	0.25
Ra_Q or Ra_{Q_T}	2.8×10^{29}	10^{30}	–	–

Table 10: Physical coefficients and parameters used in the predictions for the Earth's outer core ($\eta = 0.35$). In column GSN13 the parameters are taken from Gubbins (2001) and Pozzo et al. (2012), in A-M01 from Aubert et al. (2001), in SL05 from Shew and Lathrop (2005), and in CA06 from Christensen and Aubert (2006).

written in terms of $\dot{Q}$ is approximately $Ra_{Q_T} = 2.8 \times 10^{29}$, and $Ra_Q \approx Ra_{Q_T}$ since $Ra_c = (Ra_c)_Q$. The parameters of the table were extracted from Wijs et al. (1998), Poirier (2000), Gubbins (2001) and Pozzo et al. (2012), and the constant k refers to the thermal conductivity. On the other hand, taking into account the estimated Ekman number of the Earth's outer core $E = 2.6 \times 10^{-15}$ and that $Ra_Q^* = Ra_Q E^3 \sigma^{-2}$, it results that $Ra_Q^* = 5.0 \times 10^{-13}$, which approximately doubles 2×10^{-13} (already written in our non-dimensional units) estimated by Christensen and Aubert (2006) from the scaling of $\overline{Ro}$.

From Ra_Q^*, the mean Reynolds and Rossby numbers, $\overline{Re}$ and $\overline{Ro}$, respectively, the mean dimensional velocity $\overline{U} = (\nu/d)\overline{Re}$, together with their poloidal, $\overline{U_p}$, and axisymmetric, $\overline{U_a}$, contributions, and the mean zonal flow $|\langle \overline{v_\varphi} \rangle^d|$ at $r = r_i + (r_o - r_i)/7$ and $\theta = 3\pi/8$ can be estimated. They are included in Table 11. In addition their orders of magnitude are compared with the global Reynolds number, Re^A, the dimensional r.m.s. radial velocity, $\tilde{\sigma}_{v_r}^d$, and the dimensional local mean zonal flow, $|\overline{v_\varphi}|^d$, obtained by Aubert et al. (2001), also with the convective-based Reynolds number, Re^S, and the convective dimensional velocity, U^S, given by Shew and Lathrop (2005), and finally with the dimensional, U^{CA}, and zonal, U_z^{CA}, velocities of Christensen and Aubert (2006) (see also Tables 10 and 11).

Equation (15) gives $\overline{Ro} = 6.6 \times 10^{-5}$, which is more than one order of magnitude greater than that obtained by Christensen and Aubert (2006) with magnetic field, and with $\overline{Ro} = \overline{Re}E$, $\overline{Re} \approx 10^{10}$ is obtained. It is two orders of magnitude larger than $Re^A \approx 10^8$. One of the sources of this difference is that our Ekman number is one order of magnitude smaller. However, our results agree with theirs by considering only the poloidal part of the velocity field as a measure of the convective flow. From Eq. (17) we obtain $\overline{Re_p} \approx 3.0 \times 10^9$, and taking into account the values of ν and d given in Table 10, our dimensional poloidal velocity gives $\overline{U_p} \approx 1.3 \times 10^{-3}$ m/s, which is of the same order as $\tilde{\sigma}_{v_r}^d \sim 10^{-3}$ m/s. In contrast the convective-based Re^S is one order of magnitude smaller than ours. There is the same difference between their U^S and our $\overline{U_p}$.

Our two estimators of the strength of the zonal flows are $\overline{U_a}$ and $|\langle \overline{v_\varphi} \rangle^d|$. With $\overline{Ro_a}$ given by Eq. (19), $\overline{U_a} \approx 7.9 \times 10^{-3}$ m/s.

Property	GSN13	ABNCM01	SL05	CA06
$\overline{Re}$	10^{10}	–	–	–
$\overline{Re_p}$	10^{9}	–	–	–
Re^A	–	10^{8}	–	–
Re^S	–	–	10^{8}	–
$\overline{Re_a}$	10^{10}	–	–	–
$\overline{Ro}$	10^{-5}	–	–	–
$\overline{Ro_p}$	10^{-6}	–	–	–
$\overline{Ro_a}$	10^{-5}	–	–	–
Ro_z^C	–	–	–	10^{-7}
$Ro^{\check{C}A}$	–	–	–	10^{-6}
U^{CA} (m/s)	–	–	–	10^{-3}
$\overline{U_p}$ (m/s)	10^{-3}	–	–	–
$\overline{U_a}$ (m/s)	10^{-2}	–	–	–
U^S (m/s)	–	–	10^{-4}	–
U_z^{CA} (m/s)	–	–	–	10^{-4}
$|\langle \overline{v_\varphi} \rangle^d|$ (m/s)	$10^{-3} - 10^{-4}$	–	–	–
$|\overline{v_\varphi}|^d$ (m/s)	–	10^{-2}	10^{-4}	–
$(\sigma_{v_r}^a)^d$ (m/s)	–	10^{-3}	–	–
$\overline{U_a}/\overline{U_p}$	10	–	–	–
$|\overline{v_\varphi}|^d/U^S$	–	–	1	–
$|\overline{v_\varphi}|^d/(\sigma_{v_r}^a)^d$	–	10	–	–
Ra	10^{23}	–	10^{22}	10^{23}
Ra_Q^*	10^{-13}	–	–	10^{-13}

Table 11: Comparison of the order of magnitude of some physical properties and parameters estimated for the Earth's outer core with those of the authors of Table 10. The definitions of the physical properties are summarized in Table 12, and the super-indices A, S and C indicate values found in Aubert et al. (2001), Shew and Lathrop (2005) and Christensen and Aubert (2006), respectively.

The ratio $\overline{U_a}/\overline{U_p} \approx 6$ approaches very well $|\overline{v_\varphi}|^d/\tilde{\sigma}_{v_r}^d \approx 10$ obtained in Aubert et al. (2001). However, from geophysical observations, Jault et al. (1988) found that zonal velocities lower than the convective should be expected. The discrepancy could be due to the absence of magnetic field, which would allow stronger zonal flows. The electromagnetic stresses would tend to damp the zonal flow much more than the convective, and to reduce the azimuthal length scales. On the other hand, the dimensional mean zonal flow $|\langle \overline{v_\varphi} \rangle^d| \approx 6.3 \times 10^{-3}$ m/s, obtained from Eq. (22), is very similar to $\overline{U_a}$ despite $\overline{U_a}$ contains radial and colatitudinal contributions, and in addition it is volume-averaged. Notice that the mean zonal flow near the inner core exceeds by one order of magnitude 5×10^{-4} m/s, estimated from the westward drift of the secular variation of the magnetic field. However by taking the scaling obtained at point p_9, near the CMB, it is quite accurate. We have obtained $|\langle \overline{v_\varphi} \rangle^d| = 1.7 \times 10^{-4}$ m/s from Eq. (24). Finally, it is important to remark that the mean zonal flow, $|\langle \overline{v_\varphi} \rangle^d|$, and the poloidal velocity, $\overline{U_p}$, are of the same order. Specifically, we obtain $|\langle \overline{v_\varphi} \rangle^d|/\overline{U_p} \approx 4.8$, which is also compatible with the observations of Jault et al. (1988) if pure thermal convection is simulated.

The Rayleigh number can be estimated from Eqs. (18) and

(24) taking into account that $Ra_Q^* = RaE^2\sigma^{-1}Nu^*$. It gives $Ra = 3.6 \times 10^{23}$, which is one order of magnitude higher than that estimated in Shew and Lathrop (2005), but in very good agreement with the values of Christensen and Aubert (2006); Olson (2011). In addition, by considering Eqs. (27)-(29), the kinematic viscosity, the radial width of the Earth's outer core (see Table 10) and the above predicted Ra, a large variation of the estimated knee frequency in the core, f_c^{core}, with the radial distance, at the lowest latitudes studied (points p_7, p_8, and p_9), is obtained.

Specifically, $f_c^{core} \approx 7.2 \times 10^{-6}$ Hz near the inner boundary, 2.0×10^{-6} Hz in the middle of the shell, and 1.9×10^{-8} Hz close to the outer boundary, are found. We have obtained time scales for the convective motions ranging from 1.5 days near the inner boundary to nearly 2 years in the outer. According this result it seems that the energy is injected into the flow at different time scales depending on the radial distance. The first frequency is nearly two orders of magnitude larger than 10^{-7} given in Shew and Lathrop (2005), and calculated with the data also given in Table 10 and $Ra = 3 \times 10^{22}$, therefore their characteristic time for $\sigma = 0.010$ is 70 times higher than ours.

If f_c^{core} is associated with the time scale of the convective vortices it is possible to estimate their longitudinal length scale taking into account that $\overline{U_p} \approx 1.3 \times 10^{-3}$ m/s. It results that near the inner sphere $\delta_c^r \sim 180$ m, in the middle of the shell $\delta_c^r \sim 660$ m, and in the outer part $\delta_c^r \sim 70$ km. The latter value is almost seven times larger than the 10 Km estimated by Aubert et al. (2001) for motions near the CMB from their inertial scaling (although the convective velocities are of the same order in both studies). In addition, if the frequency of the fluctuations is due to advection of the spatial structures in the temperature field, as it is assumed in Shew and Lathrop (2005), the length scale of the structures can be estimated by using the mean zonal flow given by Eqs. (22)-(24). The velocities are $|\langle\overline{v_\varphi}\rangle^d| \approx 6.3 \times 10^{-3}$ m/s, $|\langle\overline{v_\varphi}\rangle^d| \approx 1.2 \times 10^{-3}$ m/s, and $|\langle\overline{v_\varphi}\rangle^d| \approx 1.7 \times 10^{-4}$ m/s, which gives $\delta_c^\varphi \sim 870$ m, $\delta_c^\varphi \sim 630$ m, and $\delta_c^\varphi \sim 9$ km, close to the inner boundary, in the middle of the shell, and close to the outer boundary, respectively. The length scale determined by Shew and Lathrop (2005) is $\delta_c \sim 1$ km, not much larger than our length scales near the inner boundary and in the middle of the shell, however our results near the CMB agree better with the 10 km of Aubert et al. (2001).

8. Conclusions

The numerical simulations of fully developed thermal convection of fluids filling a rotating spherical shell subject to radial heating in laboratory conditions have been compared to those of other experimental and numerical studies, either three-dimensional with stress-free boundary conditions or quasi-geostrophic with non-slip boundary conditions, and with numerical geodynamo models.

Most of our results confirm those obtained by other authors with similar parameters. The mean zonal flow, retrograde in the inner boundary and prograde in the outer near the equator, has been quantified. From Fig. 2 ($E = 10^{-4}$) the growing of

the convection can be estimated. When it is fully developed the prograde flows are confined at latitudes lower than 60° and radius larger than $r = r_i + 0.5(r_o - r_i)$. The rate of development of the polar convection from the onset is faster inside than outside the cylinder tangent to the inner boundary up to $Ra \approx 2.7Ra_c$, for which it gets a significant value.

Asymptotic power relations as a function of the parameter Ra_Q^*, independent of the diffusivities have been found. The comparison with those of Christensen (2002) and Christensen and Aubert (2006) indicates that the maximal zonal flow, generated before achieving the turbulent regimes with non-slip boundaries, represents approximately the 50% of the total kinetic energy density, while those generated with in the stress-free problem achieved 90%. On the other hand, it also shows that the inclusion of a magnetic field tends to damp the mean zonal flows more than the convective because the power law of the Nusselt number with Ra_Q^* does not change significantly.

According to the relation between the zonal and radial characteristic estimators of the velocities, three regimes are observed. The lower, of quadratic scaling between Re_t^a and Re_p, is superseded by an almost linear dependence between both Reynolds in agreement with Christensen (2002) and Gillet et al. (2007), although the quasi-geostrophic results of the latter gave a different power. Like in Shew and Lathrop (2005), evidences that the mean zonal flow saturates at the highest Ra for any $E \neq 0$ are found. This fact is consistent with the negative slope of the ratio $\overline{K/K_{na}}$. When this ratio decreases, the solutions lose their equatorial symmetry and the fully developed turbulent convection starts. This symmetry breaking has been related with the change of slope of the frequency spectra at the critical frequency f_c. Its value depends on the radius, being larger near the interior of the shell.

Finally, the fittings computed are used to extrapolate Earth's outer core values following the approach of Aubert et al. (2001), i.e. departing from the geophysically predicted total heat rate at the outer boundary. Using known values of the parameters reasonable results for the velocity field are achieved, which resemble very much those existing in the literature. For instance we have predicted mean zonal flows $|\overline{v_\varphi}|^d \approx 2 \times 10^{-4}$ m/s near the CMB, which are half the value obtained from observations. In addition we have estimated the size of the vortices of convection at different levels of the shell from $\langle\overline{v_\varphi}\rangle(r)$, U_p and $f_c(r)$, finding that it increases with the radius. Their range is $180 - 870$ m in the interior, around 660 m in the middle, and $9 - 70$ km near the CMB. Obviously, as said before the presence of the magnetic field and more realistic magnetic Prandtl numbers could change these estimations, or they could even drive geodynamo models to new regimes with unexplored energetic balances as Soderlund et al. (2012) or King and Buffett (2013) have pointed out recently.

Appendix: Definitions

Table 12 contains the parameters and definitions of the physical magnitudes used along the paper to compare with other authors. Notice that the word mean is used only to indicate time averaged quantities, while $\langle \cdots \rangle$ is left for spatial averages.

Symbol	Definition
$\mathbf{T}$	Toroidal field, $\mathbf{T} = \boldsymbol{\nabla} \times \Psi\mathbf{r}$
$\mathbf{P}$	Poloidal field, $\mathbf{P} = \boldsymbol{\nabla} \times \boldsymbol{\nabla} \times \Phi\mathbf{r}$
$\mathbf{v}$	Velocity field, $\mathbf{v} = \mathbf{T} + \mathbf{P}$
$\langle f \rangle$	Azimuthal average of f, or axisymmetric part, $\langle f \rangle(t, r, \theta) = \frac{1}{2\pi} \int_0^{2\pi} f(t, r, \theta, \varphi) d\varphi$
$\tilde{f}$	Non-axisymmetric part of f, $\tilde{f} = f - \langle f \rangle$
v_φ	Azimuthal component of the velocity field
$\langle v_\varphi \rangle$	Azimuthal average of v_φ or zonal flow
$\langle \overline{v_\varphi} \rangle$	Time average of $\langle v_\varphi \rangle$ or mean zonal flow
$\mathbf{T}_a$	Axisymmetric toroidal field, $\mathbf{T}_a = \langle \boldsymbol{\nabla} \times \Psi\mathbf{r} \rangle$
$\mathbf{T}_{na}$	Non-axisymmetric toroidal field, $\mathbf{T}_{na} = \widetilde{\boldsymbol{\nabla} \times \Psi}\mathbf{r}$
$\mathbf{P}_a$	Axisymmetric poloidal field, $\mathbf{P}_a = \langle \boldsymbol{\nabla} \times \boldsymbol{\nabla} \times \Phi\mathbf{r} \rangle$
$\mathbf{P}_{na}$	Non-axisymmetric poloidal field, $\mathbf{P}_{na} = \boldsymbol{\nabla} \times \widetilde{\boldsymbol{\nabla} \times} \Phi\mathbf{r}$
K	Kinetic energy density (KED), $K = \frac{1}{2}\langle |\mathbf{v}|^2 \rangle_{\mathcal{V}}$
K_a	Axisymmetric KED, $K_a = \frac{1}{2}\langle |\mathbf{v}_a|^2 \rangle_{\mathcal{V}}$
K_{na}	Non-axisymmetric KED, $K_{na} = \frac{1}{2}\langle |\mathbf{v}_{na}|^2 \rangle_{\mathcal{V}}$
K_t	Toroidal KED, $K_t = \frac{1}{2}\langle |\mathbf{T}|^2 \rangle_{\mathcal{V}}$
K_t^a	Axisymmetric toroidal KED, $K_t^a = \frac{1}{2}\langle |\mathbf{T}_a|^2 \rangle_{\mathcal{V}}$
K_t^{na}	Non-axisymmetric toroidal KED, $K_t^{na} = \frac{1}{2}\langle |\mathbf{T}_{na}|^2 \rangle_{\mathcal{V}}$
K_p	Poloidal KED, $K_p = \frac{1}{2}\langle |\mathbf{P}|^2 \rangle_{\mathcal{V}}$
K_p^a	Axisymmetric poloidal KED, $K_p^a = \frac{1}{2}\langle |\mathbf{P}_a|^2 \rangle_{\mathcal{V}}$
K_p^{na}	Non-axisymmetric poloidal KED, $K_p^{na} = \frac{1}{2}\langle |\mathbf{P}_{na}|^2 \rangle_{\mathcal{V}}$
Re_*	Reynolds number, $Re_* = \sqrt{2K_*}$
Ro_*	Rossby number, $Ro_* = Re_* E$
U_*	Estimated dimensional velocities, $U_* = \nu Re_*/d$

Table 12: Summary of symbols and definitions for the output data used. The symbol $*$ means the type of KED used in the definitions of *Re* and *Ro*, and in *U*.

Aubert, J., 2005. Steady zonal flows in spherical shell fluid dynamos. J. Fluid Mech. 542, 53–67.

Aubert, J., Brito, D., Nataf, H.-C., Cardin, P., Masson, J.-P., 2001. A systematic experimental study of rapidly rotating spherical convection in water and liquid gallium. Phys. Earth Planet. Inter. 128, 51–74.

Aurnou, J., Heimpel, M., 2004. Zonal jets in rotating convection with mixed mechanical boundary conditions. Icarus 169 (2), 492–498.

Aurnou, J., Heimpel, M., Wicht, J., 2007. The effects of vigorous mixing in a convective model of zonal flow on the ice giants. ICARUS 190, 110–126.

Aurnou, J. M., 2007. Planetary core dynamics and convective heat transfer scaling. Geophys. Astrophys. Fluid Dynamics 101 (5–6), 327–345.

Aurnou, J. M., Olson, P., 2001. Strong zonal winds from thermal convection in a rotating spherical shell. Geophys. Res. Lett. 28 (13), 2557–2559.

Cardin, P., Olson, P., 1994. Chaotic thermal convection in a rapidly rotating spherical shell: consequences for flow in the outer core. Phys. Earth Planet. Inter. 82, 235–259.

Christensen, U., 2002. Zonal flow driven by strongly supercritical convection in rotating spherical shells. J. Fluid Mech. 470, 115–133.

Christensen, U., Aubert, J., 2006. Scaling properties of convection-driven dynamos in rotating spherical shells and application to planetary magnetic fields. Geophys. J. Int. 166, 97–114.

Dormy, E., Soward, A. M., Jones, C. A., Jault, D., Cardin, P., 2004. The onset of thermal convection in rotating spherical shells. J. Fluid Mech. 501, 43–70.

Figueroa, A., Schaeffer, N., Nataf, H. C., Schmitt, D., 2013. Modes and instabilities in magnetized spherical Couette flow. J. Fluid Mech. 716, 445–469.

Garcia, F., Net, M., García-Archilla, B., Sánchez, J., 2010. A comparison of high-order time integrators for the Boussinesq Navier-Stokes equations in rotating spherical shells. J. Comput. Phys. 229, 7997–8010.

Garcia, F., Sánchez, J., Net, M., 2008. Antisymmetric polar modes of thermal convection in rotating spherical fluid shells at high Taylor numbers. Phys. Rev. Lett. 101 (19), 194501.

Gillet, N., Brito, D., Jault, D., Nataf, H.-C., 2007. Experimental and numerical studies of convection in a rapidly rotating spherical shell. J. Fluid Mech. 580, 83–121.

Gillet, N., Jones, C. A., 2006. The quasi-geostrophic model for rapidly rotating spherical convection outside the tangent cylinder. J. Fluid Mech. 554, 343–369.

Grossmann, S., Lohse, D., 2000. Scaling in thermal convection: a unifiying theory. J. Fluid Mech. 407, 27–56.

Gubbins, D., 2001. The Rayleigh number for convection in the Earth's core. Phys. Earth Planet. Inter. 128, 3–12.

Jault, D., Gire, G., Le Mouël, J., 1988. Westward drift, core motions and exchanges of angular momentum between core and mantle. Nature 333, 353–356.

Julien, K., Rubio, A. M., Grooms, I., Knobloch, E., 2012. Statistical and physical balances in low rossby number rayleigh-bénard convection. Geophys. Astrophys. Fluid Dynamics 106 (4–5), 392–428.

King, E., Buffett, B., 2013. Flow speeds and length scales in geodynamo models: The role of viscosity. Earth and Planetary Science Letters 371–372, 156–162.

Lister, J., Buffet, B., 1995. The strength and efficiency of thermal and compositional convection in the Earth's core. Phys. Earth Planet. Inter. 91, 17–30.

Manneville, J., Olson, P., 1996. Banded Convection in Rotating Fluid Spheres and the Circulation of the Jovian Atmosphere. Icarus 112 (2), 242–250.

Morin, V., Dormy, E., 2006. Dissipation mechanisms for convection in rapidly rotating spheres and the formation of banded structures. Phys. Fluids 18, 068104–1–068104–4.

Net, M., Garcia, F., Sánchez, J., 2008. On the onset of low-Prandtl-number convection in rotating spherical shells: non-slip boundary conditions. J. Fluid Mech. 601, 317–337.

Net, M., Garcia, F., Sánchez, J., 2012. Numerical study of the onset of thermosolutal convection in rotating spherical shells. Phys. Fluids 24, 064101–1–064101–21.

Olson, P., 2011. Laboratory Experiments on the Dynamics of the Core. Phys. Earth Planet. Inter. 187, 139–156.

Plaut, E., Lebranchu, Y., Simitev, R., Busse, F. H., 2008. Reynolds stresses and mean fields generated by pure waves: applications to shear flows and convection in a rotating shell. J. Fluid Mech. 602, 303–326.

Poirier, J. P., 2000. Introduction to the physics of the Earth's interior. Second edition. Cambridge University Press, Cambridge.

Pozzo, M., Davies, C., Gubbins, D., Alfè, D., 2012. Thermal and electrical conductivity of iron at earth's core conditions. Nature 485 (7398), 355–358.

Schmitt, D., Alboussière, T., Brito, D., Cardin, P., Gagnière, N., Jault, D., Nataf, H. C., 2008. Rotating spherical Couette flow in a dipolar magnetic field: experimental study of magneto-inertial waves. J. Fluid Mech. 604, 175–197.

Shew, W. L., Lathrop, D. P., 2005. Liquid sodium model of geophysical core convection. Phys. Earth Planet. Inter. 153, 136–149.

Shraiman, B. I., Siggia, E. D., 1990. Heat transport in high-rayleigh-number convection. Phys. Rev. A 42, 3650–3653.

Soderlund, K. M., King, E. M., Aurnou, J. M., 2012. The influence of magnetic fields in planetary dynamo models. Earth and Planetary Science Letters 333–334, 9–20.

Stelzer, Z., Jackson, A., 2013. Extracting scaling laws from numerical dynamo models. Geophys. J. Int. 193 (3), 1265–1276.

Tilgner, A., Busse, F., 1997. Finite amplitude convection in rotating spherical fluid shells. J. Fluid Mech. 332, 359–376.

Wijs, G. A. d., Kresse, G., Vočadlo, L., Dobson, D., Alfè, D., Gillan, M. J., Price, G. D., 1998. The viscosity of liquid iron at the physical conditions of the Earth's core. Nature 392, 805–807.